science.sciencemag.org/content/364/6440/566/suppl/DC1

Supplementary Material for

Particulate methane monooxygenase contains only mononuclear copper centers

Matthew O. Ross, Fraser MacMillan, Jingzhou Wang, Alex Nisthal, Thomas J. Lawton, Barry D. Olafson, Stephen L. Mayo, Amy C. Rosenzweig*, Brian M. Hoffman*

*Corresponding author. Email: amyr@northwestern.edu (A.C.R.); bmh@northwestern.edu (B.M.H.)

Published 10 May 2019, *Science* **364**, 566 (2017)
DOI: 10.1126/science.aav2572

This PDF file includes:

Materials and Methods

Production of $^{63}CuSO_4$

50 mg aliquots of ^{63}CuO (Cambridge Isotope Laboratories) were dissolved in 1.5 mL of 3 M trace metal grade H_2SO_4 while heating at 60-80°C and shaking at 300 rpm. The reaction was judged to be complete when no black CuO particles were visible in the blue $CuSO_4$ solution (after several days).

Growth of *M. capsulatus* (Bath) and preparation of Vivo-pMMO EPR sample

Isotopically enriched ^{63}Cu, ^{15}N-*M. capsulatus* (Bath) was grown in a 12 L bioreactor as described previously with minor modifications (*13, 23*). Briefly, cells were grown in a solution of 3.9 mM phosphate buffer, pH 6.8, 40 µM NaFe(III)EDTA, trace element solution, 50 µM $^{63}CuSO_4$ and 1X ^{15}N-nitrate mineral salts (NMS) (Cambridge Isotopes Laboratories, potassium ^{15}N-nitrate) with a constant flow of 1:4 methane-to-air gas mix. NaOH and H_2SO_4 were used to maintain the growth medium pH between 6.7 and 7.4. Cells were harvested by centrifugation (6,000 x g for 20 min at 4°C) at OD_{600} of 11.3. Of this yield, 0.75 g of cell pellet was set aside on ice, while the rest was frozen in liquid nitrogen and stored at -80°C. To prepare whole cell EPR samples, the 0.75 g of cell pellet was resuspended in 50 mL of 12.2 mM dibasic sodium phosphate, 7.8 mM monobasic sodium phosphate, 5 mM magnesium chloride, pH 7.0 and centrifuged at 4°C, 10,000 x g, for 10 min, as done previously (*49*). The supernatant was poured off, the wash and centrifugation procedure was repeated, and the supernatant was again poured off. The cells were resuspended in 200 µL of phosphate buffer, and this suspension was then aliquoted into a Wilmad quartz X-band EPR tube (Sigma Aldrich) and custom quartz Q-band EPR tube (~180 µL and ~80 µL, respectively, as with all EPR samples in this study). EPR samples were frozen in liquid nitrogen, where they were stored until analysis. Natural abundance *M. capsulatus* (Bath) was grown and harvested under similar conditions except natural abundance $CuSO_4$ and NMS were used for the growth medium instead of $^{63}CuSO_4$ and ^{15}N-NMS.

pMMO purification and X-band Continuous Wave (CW) and Q-band EPR/ENDOR sample preparation

M. capsulatus (Bath) cells were resuspended in 25 mM PIPES, 250 mM NaCl, pH 7.2-7.3 and lysed by sonication (either using 90% power setting, 1 s on, 1 s off sonication for 10 min, or a 90% power setting, 1 s on, 2 s off sonication for 8 min) and membranes containing pMMO were isolated, solubilized, and purified by size exclusion chromatography (using a 120 mL Superdex 200 equilibrated in 25 mM PIPES, 250 mM NaCl, 0.02 % DDM, pH 7.2-7.3, 1 mL/min flow rate) as described previously (*13, 50*), although for this study the solubilized membranes were concentrated to 2 mL (rather than 1 mL) before running size exclusion chromatography and the PIPES buffer used throughout (i.e. with and without DDM) was kept at pH 7.2-7.3 (rather than pH 7.0). After size exclusion chromatography, the sample was concentrated via centrifugation at 5,000 x g, at 4°C using a 100 kDa cutoff Amicon spin concentrator; samples were subsequently either frozen in liquid nitrogen and stored at -80°C until use, or, to make Purified-pMMO EPR samples, aliquoted into X- or Q-band EPR tubes and frozen in liquid nitrogen. To generate Reduced/Purified-pMMO, Purified-pMMO was degassed and made anaerobic on a Schlenk line, and then brought into a Coy anaerobic glovebox. 10-12 protein equivalents of sodium ascorbate in anaerobic 25 mM PIPES, pH 7.5 or 25 mM PIPES, 250 mM NaCl, 0.02 % DDM, pH 7.5 were added to the protein solution. Reduced/Purified-pMMO samples were allowed to equilibrate for at least 1 hr at room temperature in the glovebox before being aliquoted into X- or Q-band EPR tubes

which were frozen in liquid nitrogen in the glovebox. While the Cu_C(II) EPR signal was always significantly more diminished by ascorbate reduction than the Cu_B(II) signal, occasionally some Cu_C(II) was apparent even after this procedure. When this occurred, the sample was thawed anaerobically, and ascorbate was added until the Cu_C(II) signal was no longer evident. For Purified-pMMO in D_2O samples, the protein was buffer exchanged into 25 mM PIPES, 250 mM NaCl, 0.02% DDM buffer in D_2O (99.9%-D, Sigma-Aldrich), pD 7.3. To prepare Reduced/Purified-pMMO in D_2O, Purified-pMMO in D_2O was anaerobically reduced as above except the ascorbate was prepared in the deuterated buffer mentioned above (made anaerobic). Unless otherwise noted, the concentrations of all EPR/ENDOR samples of Purified- or Reduced/Purified-pMMO were comparable, only varying between 300 and 500 μM.

For Purified-pMMO incubated with nitrite, $NaNO_2$ was dissolved in 25 mM PIPES, 250 mM NaCl, 0.02% DDM, pH 7.2 to generate a 4 M $NaNO_2$ stock solution. An equal volume of this stock and natural abundance Purified-pMMO were mixed, and the sample was incubated at room temperature for 2 hr and 15 min. The sample was then transferred to either an X-band or Q-band EPR tube and flash frozen in liquid nitrogen.

For Purified- and Reduced/Purified-pMMO samples incubated with $H_2{}^{17}O$, the enzyme was desalted into 2X wash buffer (50 mM PIPES, 500 mM NaCl, 0.04% DDM, pH 7.2) using a PD-10 desalting column at 4°C. The protein was concentrated to 90 μL, ~630 μM protein using a 100 kDa cutoff Amicon filter. The protein was then diluted with 90 μL of 90% ^{17}O-enriched H_2O (Sigma Aldrich). To generate the Purified-pMMO in $H_2{}^{17}O$, 80 μL of this sample was put in a Q-band EPR tube inside of a cryotube, parafilmed to make airtight, and then left in the dark at room temperature overnight. To generate the Reduced/Purified-pMMO, with the remaining 100 μL of pMMO, the protein was made anaerobic using a Schlenk line and brought into the glovebox, where it was treated with 12 protein equivalents of ascorbate (in anaerobic 25 mM PIPES, 250 mM NaCl, 0.02% DDM, pH 7.2). The protein was incubated overnight in the dark at room temperature in the glovebox. In the morning this sample was transferred to a Q-band EPR tube. Both Q-band samples were flash frozen in liquid nitrogen in the morning (the anaerobic sample was flash frozen in the glovebox).

Design, expression, and purification of spmoB constructs and NeMCO

spmoB was recombinantly expressed in *E. coli* into inclusion bodies and refolded in 20 mM Tris, 250 mM NaCl, pH 8.0 as described previously (*27*), except Tris base was used instead of Tris-Cl.

To optimize spmoB solubility and create a solubly expressing spmoB construct, we redesigned the artificial flexible linker that connects PmoB subdomain 1 (PmoB D1) and subdomain 2 (PmoB D2) in spmoB, and tested various combinations of N- and C-terminal soluble tag attachments to spmoB. To reduce flexibility and aggregation propensity, the original linker in spmoB was replaced with the following sequence: PmoB(residues 173-182)-GEPS-Protein GB1-GE-PmoA(residues 170-203)-S, which is followed by the D2 domain starting with PmoB residue 267 (Fig. S9), in which Protein GB1 is the B1 domain of Protein G. Solubility improvements were screened by the split-GFP assay and confirmed by SDS-PAGE (*51*). Out of the screened variants, constructs Con7 with a Set12 tag (Set12 is is the T7B9 peptide (*52*)) at both C- and N-termini, and SUMO7 (Con7 with an additional N-terminal SUMO tag) were identified to be solubly expressed at ≥10 mg/L in *E. coli* (Fig. S9). In order to test whether the foldedness of the copper-binding PmoB D1 affects the activity, error-prone PCR was performed on the PmoB D1 subdomain alone, and the resulting variants were selected by a twin-arginine translocation (TAT) pathway-based

ampicillin survival assay, which has been shown to isolate variants with improved folding (*53, 54*). From this assay, a single amino acid mutation variant (PmoB D1_E75D) was identified to grant host expression *E. coli* cells with improved ampicillin survival rate than PmoB D1_WT, and assembled back to the SUMO7 construct to create SUMO7_E75D. To validate that methanol produced in the methane oxidation activity assays was a result of enzymatic turnover at the previously reported pMMO active site (Cu_B), we produced two negative control constructs which should have exhibited no methane oxidation activity. For SUMO7_3A, the three Cu_B residues (H33, H137, and H139) were mutated to alanine to abrogate copper binding at this site. The second negative control was a multicopper oxidase (NeMCO, derived from *Nitrosomonas europaea*)(*55*) that does not oxidize methane.

SUMO7, SUMO7_E75D, SUMO7_3A, and NeMCO were expressed in chemically-competent *E. coli* BL-21(DE3)Gold cells by either auto induction or IPTG induction. For auto induction, 5 mL of overnight culture in LB with 100 µg/mL of ampicillin (Amp100) was inoculated into1 L of ZYM-5052 media with Amp100 at 37℃ until OD_{600} hit 0.5, and then at 20℃ for 24 hours to express protein (*56*). For IPTG induction, 1 L of LB/Amp100 was inoculated by 5 mL of overnight culture at 37℃, and induced by 1 mM IPTG at OD_{600} between 0.6 and 1.0. Expression was then conducted at 27℃ for 4 hours. Post-expression culture was transferred to a capped bottle, supplemented with water to replace the headspace gas, and treated with 1x ZYM-5052 sugar solution together with 1 mM of $CuSO_4$ for 2 hours to allow *in-vivo* copper loading (*56*). Cells were then harvested, lysed by a cell disruptor, and centrifuged at 15,000 x g for 40 min. Soluble protein was then purified by Strep-Tactin beads (IBA) and stored in either 1x PBS (137 mM NaCl, 2.7 mM KCl, 10 mM Na_2HPO_4, 1.8 mM KH_2PO_4, pH 7.4) or 1x TBS (50 mM Tris, 150 mM NaCl, pH 7.6). Protein was concentrated by 30kDa MWCO spin-filters (Amicon) to ≤ 1 mL volume before further analysis.

For the refolded SUMO7 sample, soluble protein was expressed in C41(DE3) chemically competent *E. coli* cells in ZYM-5052 autoinduction media with 50-100 µg/mL ampicillin at 37°C (*56*). After the OD_{600} reached ~0.5, the temperature was lowered to 18°C for overnight expression. Cells were harvested by centrifugation, frozen in liquid nitrogen and stored at -80°C until use. Cells were then thawed and resuspended in 50 mM Tris, 150 mM NaCl, pH 8.0 and lysed by sonication; cell debris was pelleted by centrifugation, and the protein was purified via Strep-Tactin column (IBA-GMBH). After purification, the protein was unfolded in 8 M urea at a protein concentration of 0.7 mg/mL (protein concentration determined using the Pierce™ 660 nm assay (VWR International) and a molecular weight of 69.292 kDa) and was subsequently refolded in the presence of $CuSO_4$ following a previously described protocol (*24*). After refolding, the protein was ultracentrifuged for 40 min at 125,000 x g, 4°C, and concentrated using a 10 kDa cutoff Amicon spin concentrator. Aliquots of 50 µM SUMO7 were then immediately tested for methane oxidation activity, and the rest of the protein was frozen in liquid nitrogen and stored at -80°C until later use. To prepare the refolded SUMO7 X-band EPR sample, protein was thawed, concentrated using an Amicon spin concentrator to 250 µM, transferred to a Wilmad quartz X-band EPR tube and frozen in liquid nitrogen.

Optical spectroscopy

All optical spectroscopy measurements were performed on an Agilent 8453 spectrophotometer with an Agilent 89090A Peltier temperature controller.

Methane oxidation activity assays

All Purified- and Reduced/Purified-pMMO preparations used to produce paramagnetic resonance spectroscopy samples were verified as active (capable of catalyzing methane oxidation) using a very slightly adjusted bicelle-reconstitution ^{13}C methane oxidation activity assay (*13*). Duroquinol was generated from duroquinone (VWR International) as described previously (*25*). For all methane oxidation activity assays, 100 µL of 2.6-8.0 mg/mL purified pMMO in 3-6% DMPC:CHAPSO 2.8:1 bicelle solution (Molecular Dimensions or Anatrace), or 100 µL of spmoB/spmoB construct (concentrations and length of reaction provided in figures), were mixed with a small scoop of duroquinol placed into sealed septa top vials (Agilent). A 2:1 ratio of ^{13}C-methane (Sigma-Aldrich) and air, totaling 3 mL, was injected into the top. Reactions were incubated in a water bath shaking at 200 rpm (at least 5 min at 30°C for pMMO, otherwise temperature and time of reaction are provided in figures) after which point the reactions were either immediately stopped using 500 µL of chloroform spiked with 1 mM dichloromethane or were frozen and later thawed; upon thawing 500 µL of chloroform spiked with 1 mM dichloromethane was added to the vial. The amount of $^{12/13}$C-methanol after reaction was determined using a PoraBOND Q column (Agilent) on an Agilent 7890B/5977A MSD GC/MS instrument monitoring the 33 m/z ion (^{13}C-methanol) and 31 m/z ion (^{12}C-methanol) relative to the 49 m/z ion (dichloromethane internal standard) as described previously (*13*). The GC oven temperature holding times were varied to adjust for changing retention times over the life of the GC column. Absolute ^{13}C-methanol concentrations were determined by comparison of ^{13}C-methanol peak intensities to those of known concentration ^{13}C-methanol (Sigma-Aldrich) standards in buffer. A signal-to-noise cutoff of 1.0 for the ^{13}C-methanol integrated peak area was used to distinguish real signal from noise; samples with signal-to-noise less than 1.0 were treated as 0 µM ^{13}C-methanol.

X-band CW-EPR and Q-band ENDOR measurements

All CW X-band EPR measurements (except those of SUMO7) were performed using a Bruker ESP-300 spectrometer with a liquid helium flow Oxford Instruments ESR-900 cryostat. SUMO7 EPR was measured on a modified Varian E-4 with a liquid nitrogen finger-dewar at 77 K. All wide scans spanning ≥1000 G were background subtracted. Collection conditions (Fig. 1, wide and inset scans): 9.36-9.37 GHz microwave frequency, 90 s per scan, 320 ms time constant, 12.5 G modulation amplitude, temperature at 20 K, at least 5 scans. SI spectra collection conditions are provided below the figures. All EPR simulations were performed using EasySpin (*57*).

Pulsed ENDOR measurements were collected at ~2 K in a liquid helium immersion dewar on a spectrometer described elsewhere, with SpinCore PulseBlaster ESR_PRO 400MHz digital word generator, and Agilent Technologies Acquiris DP235 500 MS/sec digitizer using SpecMan software (*58, 59*). For all ^{1}H and strongly-coupled ^{15}N ENDOR measurements, a Davies [π–T_{RF}–$\pi/2$–τ–π–τ–echo] pulse sequence was employed, in which T_{RF} denotes the interval during which the RF was applied. For weakly-coupled remote ^{15}N ENDOR measurements, a Doan/ReMims [$\pi/2$–τ_1–$\pi/2$–T_{RF}–$\pi/2$–τ_2–π–(τ_1 + τ_2)–echo] or a Mims [$\pi/2$–τ–$\pi/2$–T_{RF}–$\pi/2$–τ–echo] pulse sequence was employed (*60*). Hyperfine coupling (A) of I = 1/2 nuclear spin (^{15}N and ^{1}H) and S = 1/2 electron spin (Cu(II)) produce an ENDOR spectrum given by the equation $v_{\pm} = |v_{\mathrm{n}} \pm \frac{A}{2}|$, where v_+ and v_- are the high and low frequency peaks of the doublet, respectively, while v_n is the Larmor frequency for the nucleus (n). For Fig. 2, collection conditions were as follows: (strongly-coupled ^{15}N) 34.592 GHz microwave frequency, 100 ms repetition time, π = 80 ns, τ = 600 ns, T_{RF} = 15 µs, and RF tail = 5 µs; (weakly-coupled ^{15}N) 34.608 GHz microwave frequency, 20 ms repetition time, π = 60 ns, τ_1 = 200 ns, τ_2 = 400 ns, T_{RF} = 60 µs, and RF tail = 10 µs, ^{15}N-Larmor

corrected. The sign of the ^{15}N hyperfine coupling was determined through the Pulsed ENDOR Saturation Recovery (PESTRE) experiment (Fig. S14), which provides the absolute sign of A/g_n (*61*).

X-band pulsed DEER sample preparation and measurements

75 µL of 360 µM natural abundance Purified-pMMO in 2X wash buffer (50 mM PIPES, 500 mM NaCl, 0.04% DDM, pH 7.2) was aliquoted into a Wilmad quartz X-band EPR tube. The altered buffer conditions do not affect the Cu(II) ligation (Fig. S15). X-band pulsed EPR spectra were recorded on a Bruker E680 spectrometer (Bruker, Rheinstetten, Germany) using a Bruker MD5-W1 EPR probehead equipped with a self-modified cryogen-free cryostat (Advanced Research Systems Inc, Macungie, PA, USA). The microwave pulses were amplified using a 1kW-TWT (Applied Systems Engineering Inc., Fort Worth, TX, USA). All EPR experiments were carried out at 17K. The field-swept spectrum was obtained by integrating the Hahn echo signal as a function of the magnetic field after a two-pulse sequence.

For the 4-pulse PELDOR experiments recorded at 17 K, pulse lengths were 20 nsec for $\pi/2$ and 20 nsec for π. The pump pulse length was 16 nsec and $\Delta\nu$ ($\nu_{obs} - \nu_{pump}$) was 80 MHz, with the detection field set at a *g* value of 2.07. The pulse separation τ_1 was 200 nsec while τ_2 varied between 2500-3500 ns, and the echo signals were integrated using a video amplifier bandwidth of 20 MHz. The pump pulse was stepped out by 16 nsec for a total number of points in T that depended upon the τ_2 used. Nuclear modulation artifacts were suppressed using a systematic variation of the interpulse delay time τ_1 and an appropriate phase cycling routine.

Supplementary Text

Discrepancy between the paramagnetic resonance analysis and previous data supporting a dicopper site

Previous EXAFS scattering was fit with a short Cu-Cu distance (~2.5-2.6 Å) indicative of a dicopper center. However, all three possible oxidation states of a dicopper center, Cu(II)-Cu(II), Cu(II)-Cu(I), or Cu(I)-Cu(I), are not consistent with the current analysis. Two Cu(II) ions at ~2.5-2.6 Å separation, with no magnetic interaction between them, would produce a large dipolar splitting in the EPR spectrum that is not observed. A (anti)ferromagnetically coupled Cu(II)-Cu(II) center would not contribute to the paramagnetic resonance spectroscopy, but we do not observe the characteristic charge transfer optical absorbance features associated with the superexchange coupling pathway requisite to forming such centers (*62, 63*). To the best of our knowledge, there is no dicopper Cu(I)-Cu(I) metal site in biology that does not oxidize in air, so if a Cu(I)-Cu(I) site were present, it would oxidize to either Cu(II)-Cu(I) or Cu(II)-Cu(II) during the aerobic purification procedure. In addition, in previous studies from our laboratory (*13, 15*), Cu(II) EPR spin quantitation of purified pMMO indicated that nearly all Cu in the protein is EPR active Cu(II), inconsistent with a dicopper Cu(I)-Cu(I) site. Finally, we consider a Cu(II)-Cu(I) center. As noted previously, we do not observe any of the characteristic features associated with such valence-delocalized center (*24*). As described in the main text, the 4 N ligands in the Cu_B site all are bound to the single Cu(II) giving rise to the Cu_B EPR signal; the terminal NH_2 and the side chains of His33, His137, and His139 are coordinated in a square plane of equatorial coordination. Thus, there are no ligands available to coordinate a second copper ion, excluding the possible presence of a valence-localized Cu(II)-Cu(I) site. Viewed from a different perspective, the Cu(II) EPR signal from spmoB differs from that of Cu_B in pMMO, yet the EXAFS for both proteins was fit with the same Cu-Cu scattering interaction (within ~0.1 Å) (*27*). It is implausible that the two samples with distinct copper centers coincidentally both contain dicopper centers with the same Cu-Cu distance. The optical absorbance feature proposed to be assignable to a dicopper site in pMMO is discussed in the caption to Fig. S5, and spmoB methane oxidation activity proposed to occur at a dicopper Cu_B site is discussed in the caption to Fig. S11.

Table S1. Summary of the paramagnetic spectroscopic parameters of the Cu_B and Cu_C sites.*

	g_1, g_2, g_3	Cu A_1, A_2, A_3 (MHz)	Directly Coord. ^{15}N A_1, A_2§ (MHz)†	Remote ^{15}N $\|A_1\|$ (MHz)		^1H A_1, A_2 (MHz)‡
Cu_B	2.242, 2.068, 2.035	570, 30, 14	-48, -54 -53, -54 -53, -54 -53, -66	1.7 2.3 2.3 N/A	His33-NH_2 $H_{\varepsilon\text{-}1}$ $H_{\varepsilon\text{-}2}$ H_β H_δ	~10, ~10 - , 4.5 - , 2.5 - , ~1 - , ~1
Cu_C	2.30, 2.07, 2.05	440, 40, 20	-48, -54 -53, -66	~2	H_xO	~8, ~10

* For simulations featuring the full Vivo-, Purified-, and Reduced/Purified-pMMO EPR spectra in Fig. 1 using the above parameters, anisotropic *g*-strain (for both Cu_B and Cu_C, EasySpin *g*-strain parameters 0, 0, 0.03 for g_3, g_2, g_1, respectively) was employed, with additional isotropic 14 G and 25 G fwhm Gaussian line width broadening for Cu_B and Cu_C, respectively. For simulations depicted in insets, the Cu_B g_1 value was changed very slightly to 2.252, and isotropic 13 G fwhm Gaussian line width broadening was employed, with no anisotropic broadening. Simulation of Purified-pMMO represents the sum of 1 Cu_B equivalent and 0.32 Cu_C equivalents. For comparison to ^{14}N ENDOR measurements, see Table S3.

§ Strongly-coupled ^{15}N A_2 ENDOR measurements are shown in Fig. S16. The four features seen in these spectra are plausibly, but not uniquely assigned as listed.

† PESTRE experiments determined that all directly-coordinated ^{15}N possess positive spin density $\rho > 0$ (Fig. S14); the ^{15}N hyperfine couplings are therefore negative because the ^{15}N nuclear $g_n < 0$.

‡ The ^1H ENDOR assignment to individual C-H/N-H bonds of the histidine imidazole ring and amine are made by analogy to Cu(II)(histidine)$_2$ complex (*34*).

Table S2. Vivo-pMMO ^{15}N A_1 Gaussian fitting parameters used in Fig. 2.*

	Resonance	Gaussian Function Parameters			R^2
Remote ^{15}N	Red		$k = 30.32$ $a_1 = 0.08824$ $b_1 = 0.8631$		0.997
	Blue§		$a_2 = 0.1194$ $b_2 = 1.149$		
Directly-coord. ^{15}N	Red		$k = 6.57$ $a_1 = 1.341$ $b_1 = 27.5$		0.9938
	Blue†	$a_2 = 1.329$ $b_2 = 32.28$	$a_3 = 1.75$ $b_3 = 31.13$	$a_4 = 0.9132$ $b_4 = 30.77$	

* The colors red or blue define the color of the Gaussian curves shown in Fig. 2, which were used to fit the ^{15}N v_+ resonance. R^2 values correspond to the fit of the full normalized Gaussian function to the experimental spectrum over a range of $v - v_{^{15}\mathrm{N}}$= 0.627-1.604 MHz for remote ^{15}N, and over a range of 25.651-28.043 MHz for directly-coordinated ^{15}N resonance. The MatLab Curve Fitting tool was used to fit the Gaussian function parameters, using the following equations: normalized Gaussian function,

remote ^{15}N: $$f(\mathrm{x}) = k\left(\frac{1}{a_1\sqrt{2\pi}}e^{-\frac{(\mathrm{x}-b_1)^2}{2(a_1)^2}} + 2\frac{1}{a_2\sqrt{2\pi}}e^{-\frac{(\mathrm{x}-b_2)^2}{2(a_2)^2}}\right),$$

directly-coordinated ^{15}N:
$$f(\mathrm{x}) = k\left(\frac{1}{a_1\sqrt{2\pi}}e^{-\frac{(\mathrm{x}-b_1)^2}{2(a_1)^2}} + \frac{1}{a_2\sqrt{2\pi}}e^{-\frac{(\mathrm{x}-b_2)^2}{2(a_2)^2}} + \frac{1}{a_3\sqrt{2\pi}}e^{-\frac{(\mathrm{x}-b_3)^2}{2(a_3)^2}} + \frac{1}{a_4\sqrt{2\pi}}e^{-\frac{(\mathrm{x}-b_4)^2}{2(a_4)^2}}\right),$$

where k is a factor that scales calculated and experimental spectra, a_n is related to the width of the peak (in MHz), and b_n defines the center of the Gaussian peak (in MHz).

§ In Fig. 2 the blue peak intensity is twice that produced by simply using the parameters to account for the fact that the function used for total fitting also doubles the intensity of this peak relative to the red peak

† Blue, directly-coordinated ^{15}N resonance function is defined by the sum of three equal area Gaussian functions

Table S3. Conversion of ^{15}N hyperfine coupling to equivalent ^{14}N hyperfine coupling for comparison with past characterization of Purified pMMO.

	^{15}N $\|A_1\|$ (MHz)		**^{14}N $\|A_1\|$ (MHz)**	**Source**
^{15}N-labelled	A_1-$^{15}N_1$	48	[*34*]†	This study
	A_1-$^{15}N_2$	53	[38]†	
Natural abundance	N/A		35.5	(*24*)

† Values in brackets correspond to hyperfine coupling predicted based on conversion between the two nuclear gyromagnetic ratios: $A_{^{15}N} = 1.403(A_{^{14}N})$, (*64*). The two distinguishable ^{15}N hyperfine couplings observed with ^{15}N-labelled Purified-pMMO are not resolved from one another in the natural abundance Purified-pMMO ^{14}N ENDOR spectrum from (*24*), presumably due to the substantial quadrupolar broadening of the ^{14}N ENDOR response.

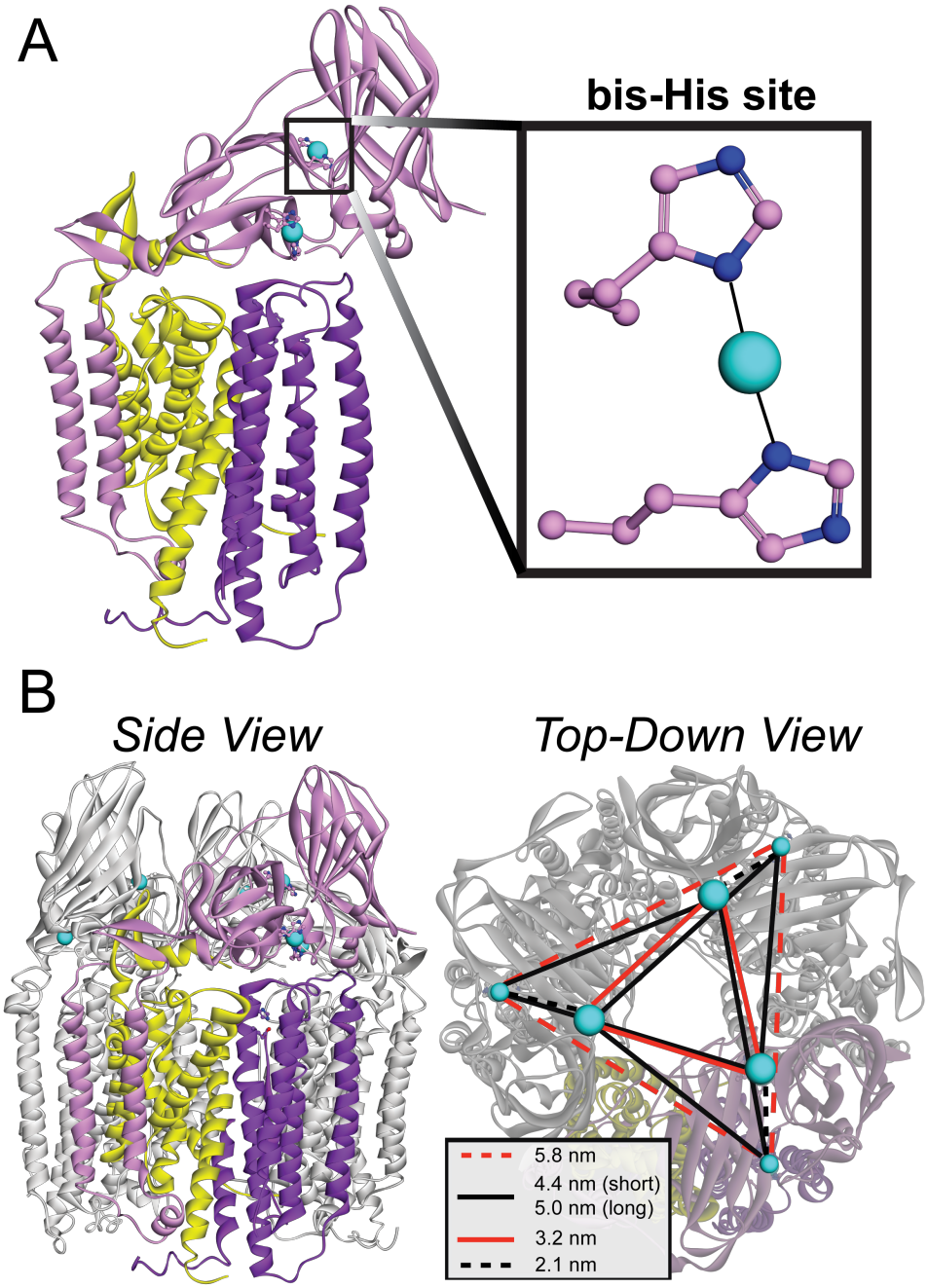

Fig. S1. (**A**) One protomer of the *M. capsulatus* (Bath) pMMO modeled with an unoccupied PmoC metal site and a Cu-bound bis-His site. ***Inset***: A closer view of the bis-His site. (**B**) Full pMMO trimer with Cu_B to bis-His Cu distances (***inset***).

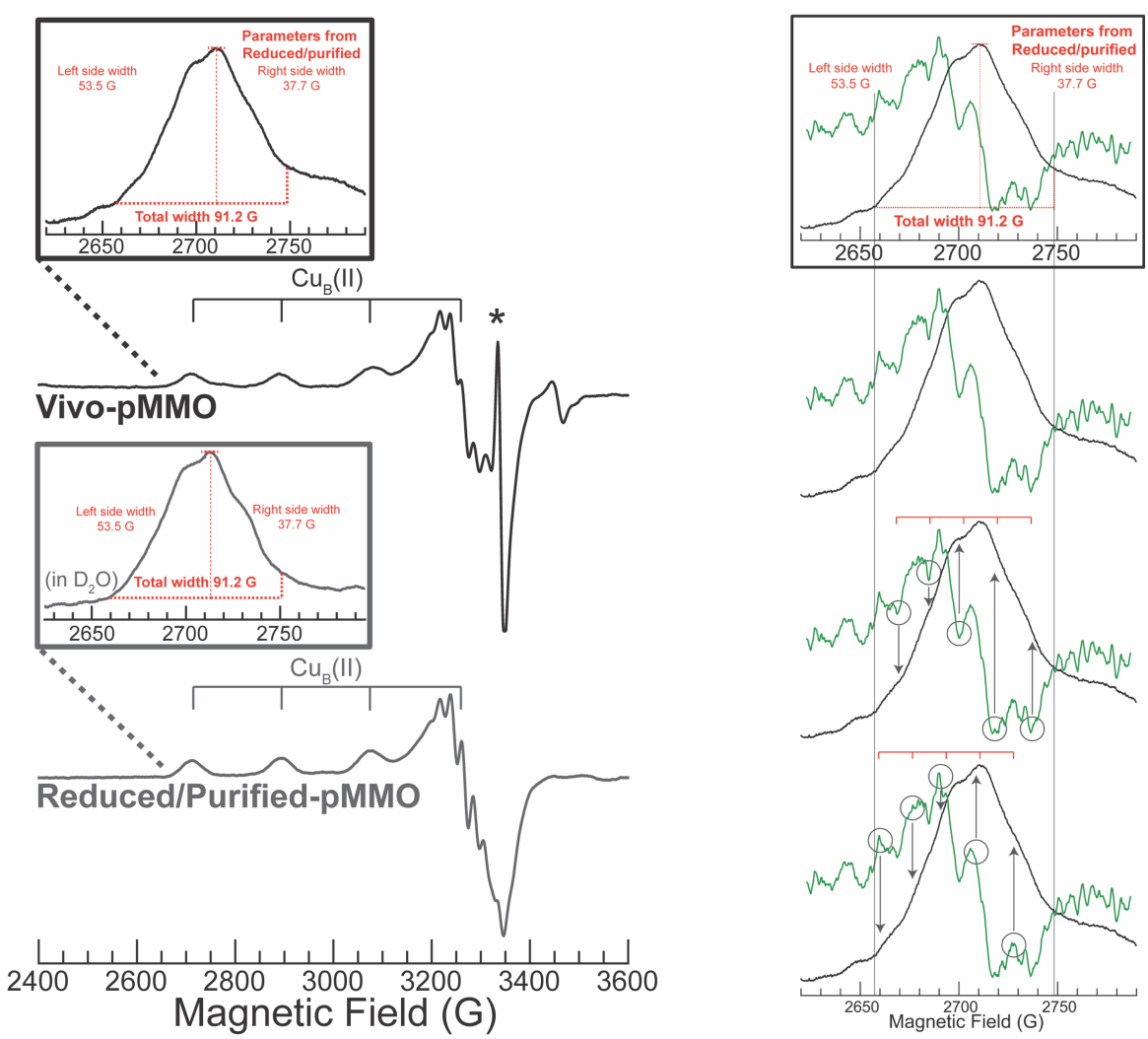

Fig. S2. Support for the assignment of 4 directly coordinated N equatorial ligands on Cu_B from the EPR shown in Fig. 1. We first distinguished the region corresponding to Cu_B(II) resonance from resonance attributable to the contaminant paramagnet(s) clearly present at the high and low field edge of the Vivo-pMMO single Cu(II) hyperfine line in this region. Toward this end, we measured the total width of the low field Cu_B(II) hyperfine line in Reduced/Purified-pMMO (left, bottom), since this spectrum does not contain these contaminants. Specifically, we measured the width of the total resonance to the left and to the right of the hyperfine transition maximum height peak. We then used these bounds to define the Cu_B(II) resonance in Vivo-pMMO (left, top and right). There are 5 evenly spaced local minima in the second derivative (green) of the experimental spectrum, as well as the 5 corresponding evenly spaced local maxima, as shown by the circles in the figure below, indicative of 5 hyperfine lines. Additionally, these peak and valley features clearly correspond to the expected splittings on the absorption-like experimental spectrum. 5 hyperfine lines can only be accounted for by 4 approximately equivalent $I = 1/2$ nuclei, such as that expected from 4 ^{15}N equatorial ligands.

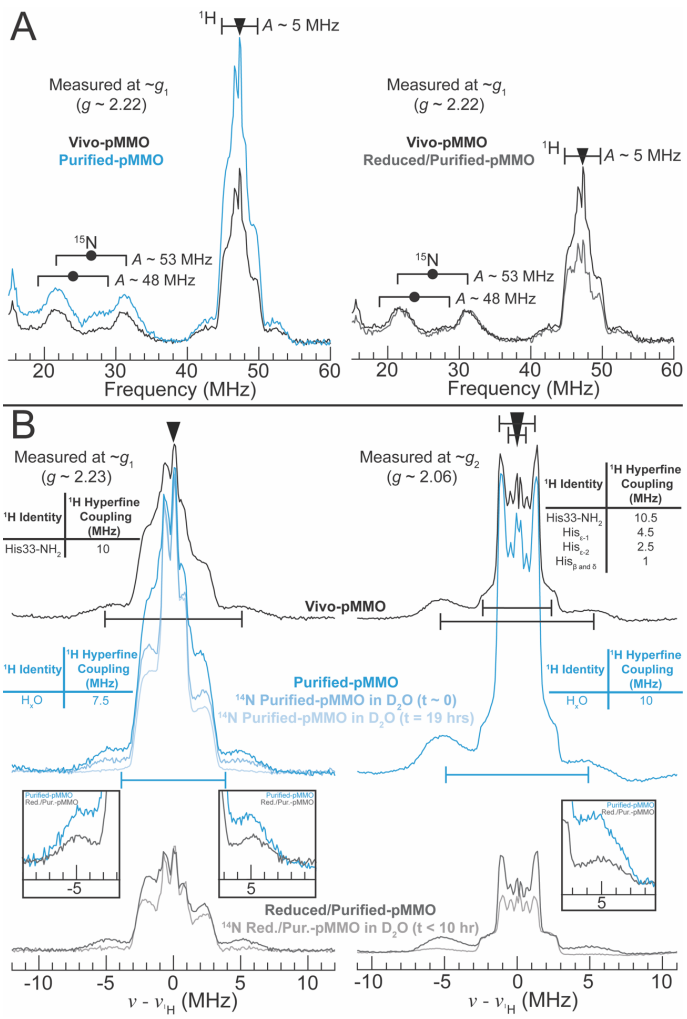

Fig. S3. ^{1}H and ^{15}N Davies ENDOR for Vivo-, Purified-, and Reduced/Purified-pMMO. Times incubated in D_2O buffer are listed. (**A**) ENDOR measurements simultaneously probing ^{15}N and ^{1}H, with heights normalized to echo intensity. Filled circle defines half the ^{15}N hyperfine coupling magnitude ($|A/2|$) and associated goalpost width indicates twice the ^{15}N Larmor frequency ($\nu_{^{15}N}$); triangle defines the ^{1}H Larmor frequency ($\nu_{^1H}$) and associated goalpost width defines hyperfine coupling magnitude ($|A|$). The weakly-coupled ^{1}H resonance (A < ~5 MHz) in Vivo-pMMO that is less intense in Reduced/Purified-pMMO is attributed to solvent H_xO near the Cu_B site in vivo that is not present in purified enzyme. Collection conditions: 34.5-34.6 GHz microwave frequency, 100 ms repetition time, π = 200 ns, τ = 600 ns, T_{RF} = 60 µs, and RF tail = 10 µs. (**B**) ^{1}H Larmor-centered ^{1}H ENDOR measured at (***left***) g_1 and (***right***) g_2, where triangle defines the ^{1}H Larmor frequency ($\nu_{^1H}$) and goalpost width defines the hyperfine coupling magnitude ($|A|$). Vivo-, Purified-, and Reduced/Purified-pMMO ENDOR intensities were normalized to ENDOR intensities in (**A**). ***Insets*** highlight the increased intensity and altered lineshape of the Purified-pMMO large coupling ^{1}H resonance relative to Reduced/Purified-pMMO, evidence for a coordinated H_xO (with hyperfine coupling, $|A_1|$ ~ 8 MHz, $|A_2|$ ~ 10 MHz) (*65*) on Cu_C. Collection conditions: 34.5-34.8 GHz microwave frequency, 100 ms repetition time, π = 200 ns, τ = 600 ns, T_{RF} = 60 µs, and RF tail = 10 µs.

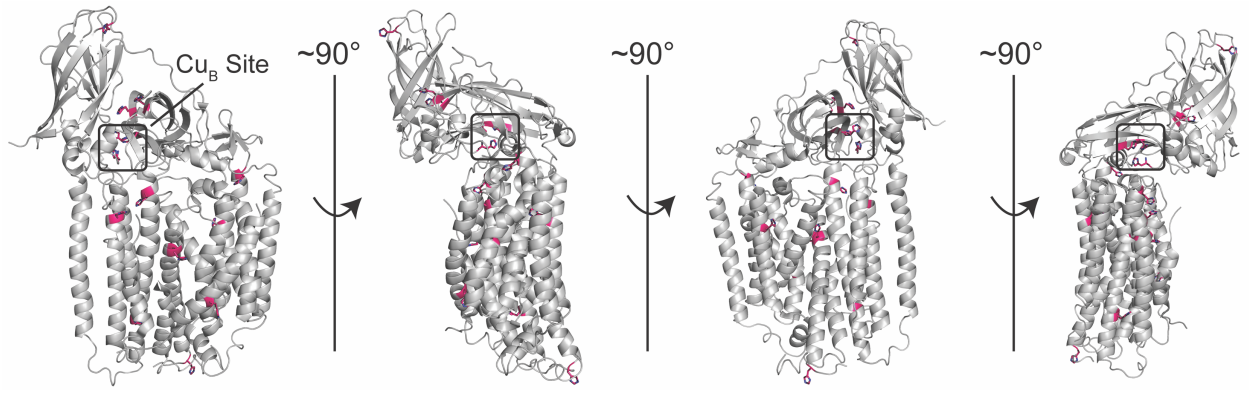

Fig. S4. One protomer of *M. capsulatus* (Bath) pMMO from the crystal structure in Fig. 1, with all protomers colored gray, shown from several angles, with His residues highlighted in pink. The Cu_B site is the only site where three His side chains come together.

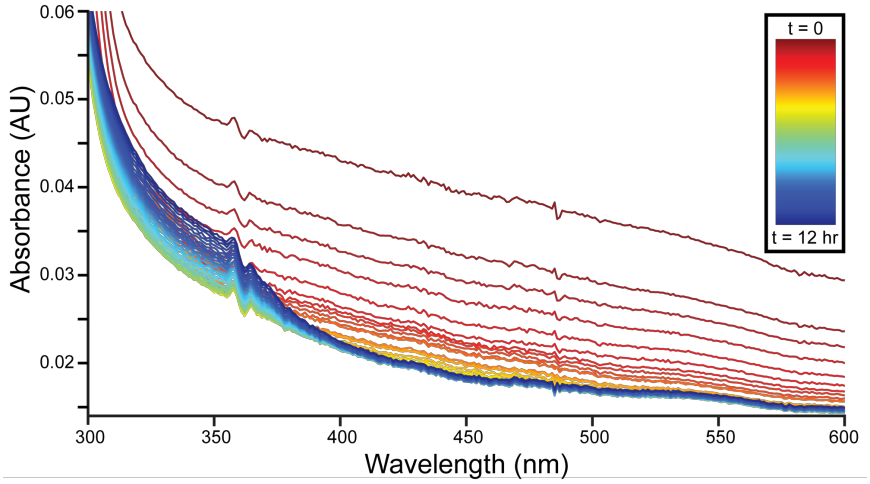

Fig. S5. UV-Vis spectra monitoring formation of the 345 nm optical feature. A sample of 25 mM PIPES, 250 mM NaCl, 0.02% DDM, pH 7.2 (*M. capsulatus* (Bath) Purified-pMMO wash buffer) with 120 µM $CuSO_4$ (to represent the Cu equivalents present in the pMMO sample used previously (*37*)) and 4 µM methanol (to represent background-level contamination present to varying degrees in most pMMO preparations) was made anaerobic in a sealed cuvette and incubated with 5 Cu(II) equivalents of ascorbate for 30 min. 2.5 Cu(II) equivalents of H_2O_2 were then added using a gas-tight syringe, and optical spectra were measured every 15 min for 12 hr at room temperature. Formation of the 345 nm feature is observed on the timescale defined previously (*37*) and can be attributed to ketal derivatives of dehydroascorbic acid generated by the reaction of ascorbate and H_2O_2 (*66*). The drifting baseline in early timepoints is an instrument artifact. The variable intensity of the 345 nm feature previously observed upon mutation of the Cu_B ligands is likely due to the strong dependence of dehydroascorbic acid ketal derivatives on trace metals for stability, since mutation of the copper binding ligands leads to lowered levels of copper in the sample. Consistent with this conclusion, close inspection of the spmoB_H137,139A (Cu_B ligating His residues mutated) optical spectrum reveals the presence of a small amount of 345 nm absorbance despite mutation of two of the three Cu_B His ligands (*37*). Conversely, the spmoB_H48N_137,139A (bis-His and Cu_B residues mutated) optical spectrum shows no evidence of 345 nm absorbance. The only difference between spmoB_H137,139A and spmoB_H48N_137,139A is mutation of the nonconserved bis-His residue His48. This mutation decreases the total amount of Cu bound by the protein by approximately 0.5 Cu equivalents (*24*). The reason this was not noted previously was likely the low intensity of the 345 nm feature in the spmoB_H137,139A optical spectrum.

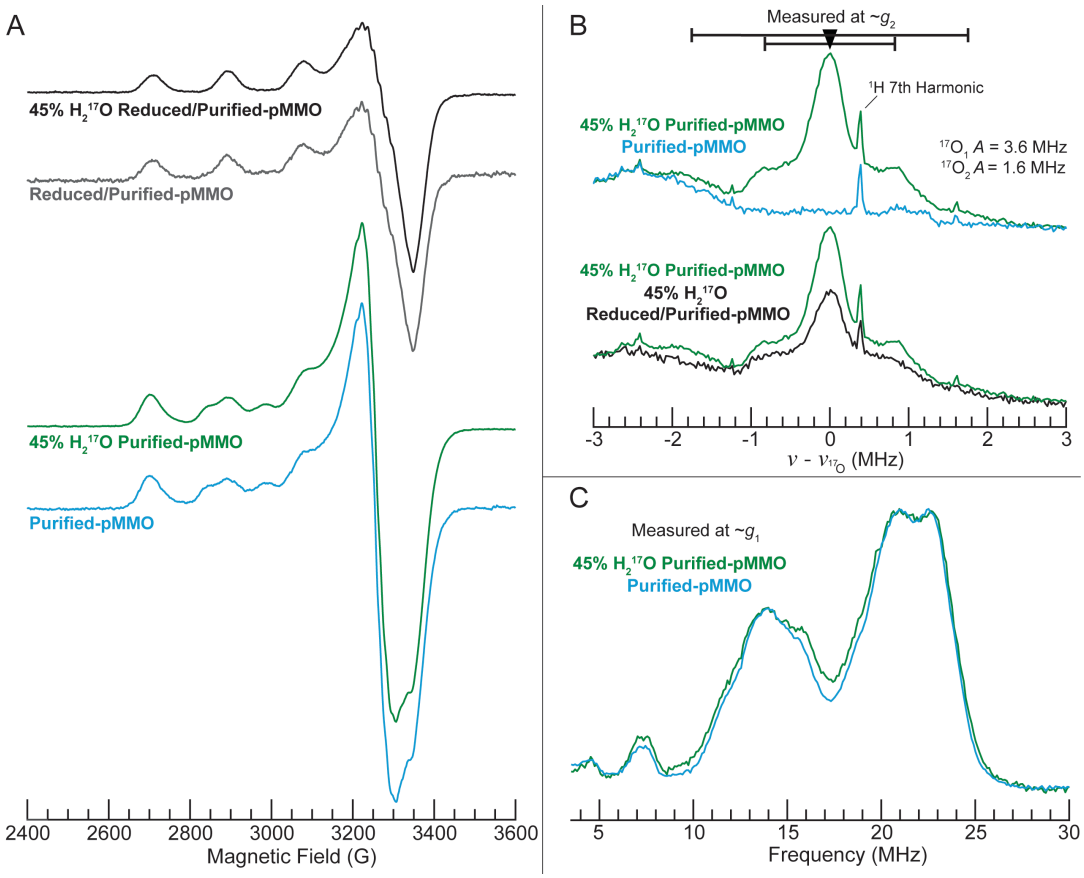

Fig. S6. EPR and ENDOR characterization of (all samples were natural abundance N and Cu) Purified- and Reduced/Purified-pMMO with $H_2{}^{17}O$. (**A**) X-band EPR measurements assessing Purified- and Reduced/Purified-pMMO, both in 45% $H_2{}^{17}O$ compared to natural abundance H_2O (~0% ^{17}O). If Cu_B(II) featured an equatorial H_xO ligand, both $H_2{}^{17}O$ Purified- and $H_2{}^{17}O$ Reduced/Purified-pMMO would exhibit broadening of the ^{14}N hyperfine lines relative to the natural abundance H_2O samples, due to the large hyperfine coupling to the ^{17}O (approximately equivalent to that of an equatorial N ligand) (*67*). However, neither sample exhibits such broadening. ***Conditions***: 9.36-9.37 GHz microwave frequency, 90 s scan rate, 320 ms time constant, 12.5 G modulation amplitude, temperature 20 K. Protein concentrations of natural abundance Purified- and Reduced/Purified-pMMO were 167 µM. (**B**) Mims ^{17}O-Larmor centered ENDOR testing for weakly-coupled ^{17}O on Cu_B and Cu_C. The ^{17}O hyperfine coupling A = 1.6 MHz observed in both $H_2{}^{17}O$ Reduced/Purified-pMMO and Purified-pMMO is of the magnitude expected for an axial H_xO ligand (*68*). Thus, there exists an axially coordinated H_2O on Cu_B. The larger coupling ^{17}O A = 3.6 is attributed to a H_xO coordinated to Cu_C. ***Conditions***: 34.6-34.7 GHz microwave frequency, 20 ms repetition time ($H_2{}^{17}O$ Purified-pMMO and natural abundance Purified-pMMO), 100 ms repetition time ($H_2{}^{17}O$ Reduced/Purified-pMMO), π = 100 ns, T_{RF} = 60 µs, τ = 1400 ns and RF tail = 10 µs. (**C**) The equivalence of the Davies ENDOR responses between natural abundance and $H_2{}^{17}O$ Purified-pMMO samples in this region indicates that Cu_B does not feature an equatorial $H_x{}^{17}O$ ligand whose coupling would be ~30-33 MHz (^{17}O Larmor frequency $\nu_{^{17}O}$ = 6.4 MHz) as shown previously (*67*). ***Conditions:*** 34.5-34.7 GHz microwave frequency, 20 ms repetition time, π = 80 ns, T_{RF} = 15 µs, τ = 475 ns, RF tail = 5 µs.

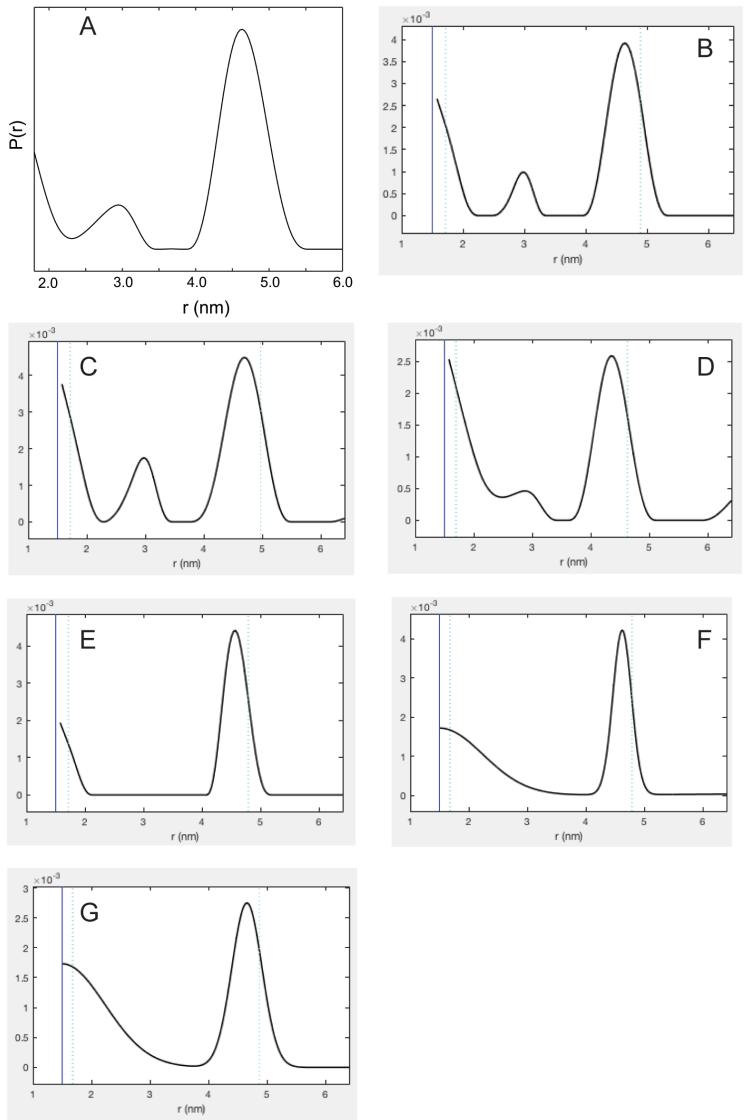

Fig. S7. Alternative analyses of DEER distance distributions showing that the feature at 4.5 nm is robust to analysis procedure, whereas the 2.8 nm feature is highly variable. The distribution shown in (**A**) is the same as that presented in Fig. 3. *Analysis procedures*: (**A**) manually optimized phase correction, zero time, using a 3rd order homogenous background function, followed by Tikhonov regularization. (**B**) Automatic phase correction, zero time, using a 2nd order homogenous background function, followed by Tikhonov regularization. (**C**) Automatic phase correction, zero time, using a 1st order polynomial background function, followed by Tikhonov regularization. (**D**) Automatic phase correction, zero time, using a 2nd order polynomial background function, followed by Tikhonov regularization. (**E**) Manually optimized phase correction, zero time, using a 2nd order homogenous background function, followed by Tikhonov regularization. (**F**) Automatic phase correction, zero time, using a 1st order polynomial background function, followed by 2 Gaussian fit function. (**G**) Automatic phase correction, zero time, using a 1st order polynomial background function, followed by 2 Gaussian homogeneous fit function.

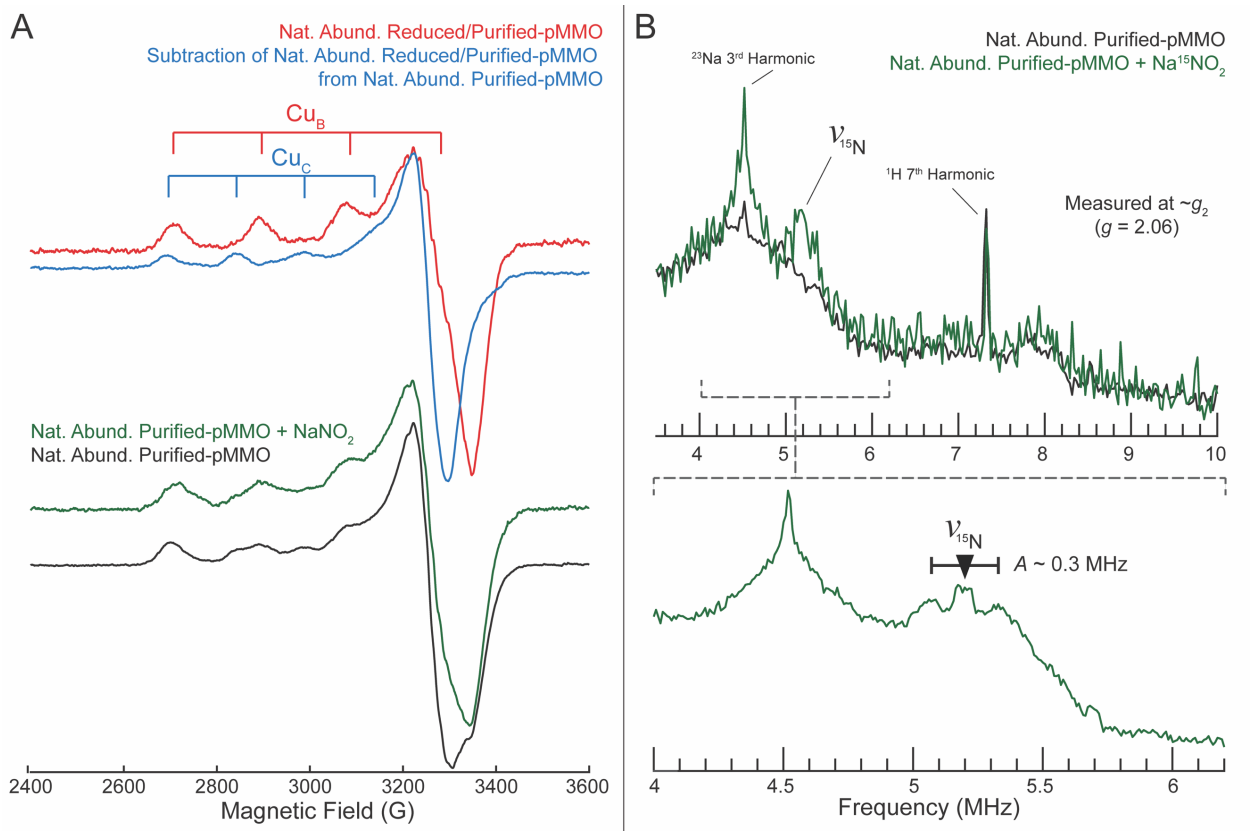

Fig. S8. Natural abundance Purified-pMMO before and after incubation with 2 M $NaNO_2$. At this concentration of $NaNO_2$, pMMO in bicelles has <25% methane oxidation activity relative to samples without $NaNO_2$. (**A**) X-band CW-EPR showing nitrite-induced changes to the Cu_C(II) EPR signal, which are most evident in the $g_\perp$ region (~3300 G), a collapse of the otherwise resolved features. ***Conditions:*** 9.365 GHz microwave frequency, 90 s scan rate, 320 ms time constant, 12.5 G modulation amplitude, temperature 20 K. Purified- and Reduced/Purified-pMMO protein concentrations were 167 µM, while the Purified-pMMO sample after nitrite incubation was 83 µM. (**B**) Q-band Mims ENDOR comparing natural abundance Purified-pMMO to natural abundance Purified-pMMO incubated with 2 M $Na^{15}NO_2$. The bottom expanded view shows the ^{15}N Larmor frequency ($\nu_{^{15}N}$) region at higher signal/noise ratio, with the resolved hyperfine coupling of the magnitude expected for $^{15}NO_2^-$ coordinated to the Cu(II) via oxygen(s) highlighted (A ~ 0.3 MHz) (*42*). Triangle defines the $\nu_{^{15}N}$ and associated goalpost width defines hyperfine coupling magnitude ($|A|$). ***Conditions:*** (top) 34.7 GHz microwave frequency, 20 ms repetition time, π = 100 ns, T_{RF} = 60 µs, τ = 1400 ns, RF tail = 10 µs, Purified-pMMO scan time = 17 min, Purified-pMMO + $Na^{15}NO_2$ scan time = 40 min; (bottom) 34.7 GHz microwave frequency, 10 ms repetition time, π = 100 ns, T_{RF} = 60 µs, τ = 1000 ns, RF tail = 10 µs, scan time = 3.5 hrs.

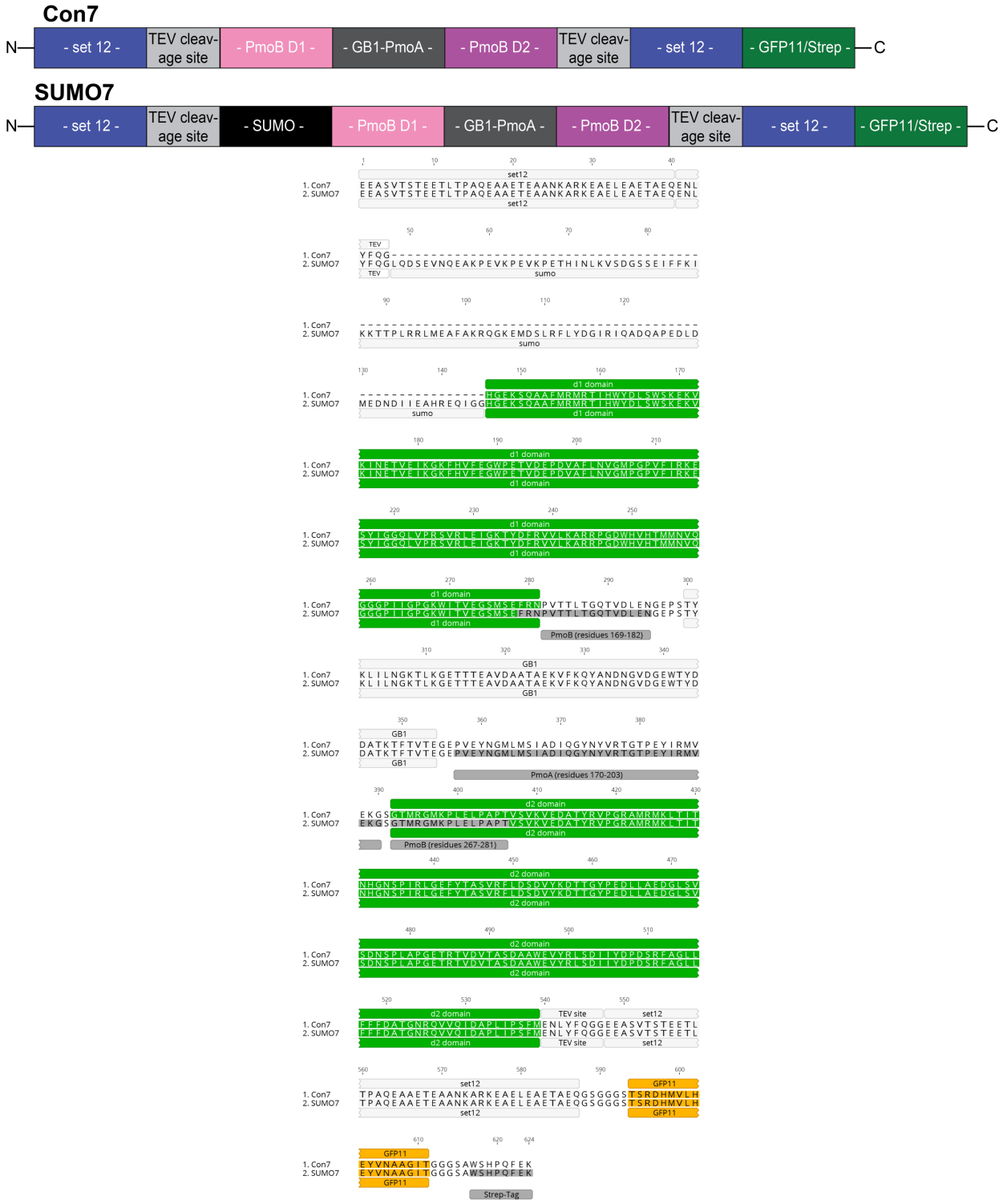

Fig. S9. Designed spmoB constructs used in ^{13}C-methane oxidation activity assays. The PmoB subdomain 1 (PmoB D1) is joined to PmoB subdomain 2 (PmoB D2) by GB1-PmoA rather than the flexible linker used to join the two subdomains in spmoB. GFP11 corresponds to the fragment of GFP utilized for the split GFP assay, and Strep refers to the Strep-tag. Figure generated with Geneious version 9.1 created by Biomatters.

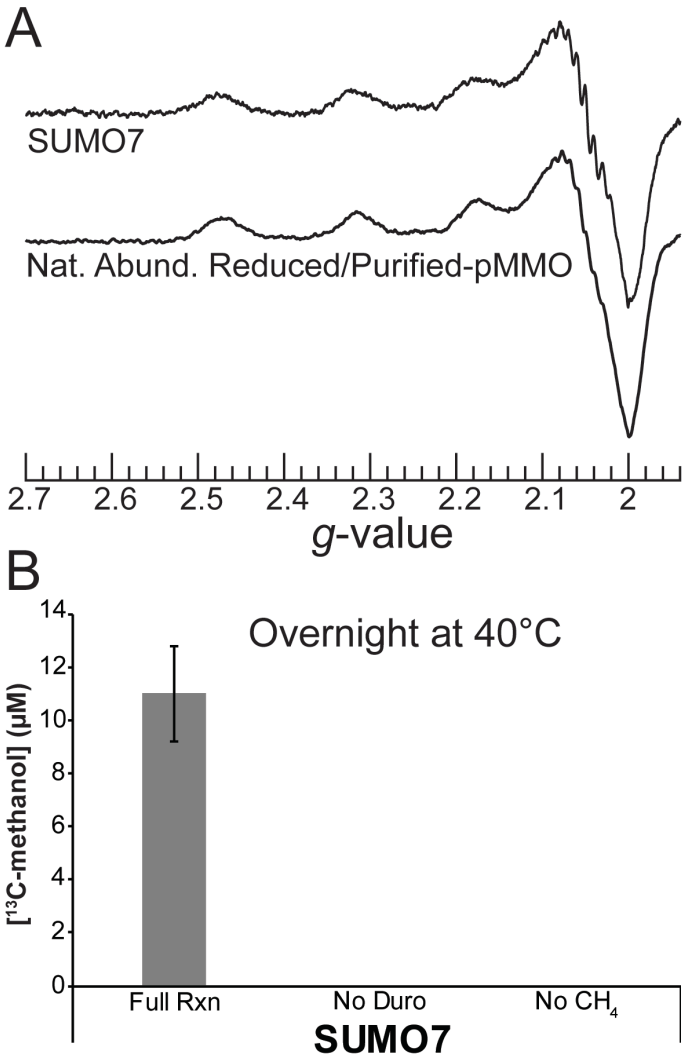

Fig. S10. Refolded SUMO7 and natural abundance Reduced/Purified-pMMO X-band EPR spectra, and SUMO7 ^{13}C-methane oxidation activity. (**A**) The inactive SUMO7 exhibits a Cu_B(II) EPR signal similar to Reduced/Purified-pMMO although the Cu_B(II) site formed in SUMO7 cannot be identical to that of Reduced/Purified-pMMO since the N-terminal residue of SUMO7 is not His33 (and thus His33 cannot coordinate via both side chain and amine). ***Conditions:*** The SUMO7 and Reduced/Purified-pMMO concentrations are 250 and 167 μM, respectively. Spectra normalized to unity. SUMO7, 9.125 GHz microwave frequency, 1 min scan rate, 30 ms time constant, 4 G modulation amplitude, 77 K temperature; natural abundance Reduced/Purified-pMMO, 9.367 GHz microwave frequency, 90 s scan rate, 320 ms time constant, 12.5 G modulation amplitude, 20 K temperature. (**B**) ^{13}C-methane oxidation activity assay of the same batch of refolded SUMO7 as probed by EPR in (**A**). The SUMO7 protein concentration was 50 μM. SUMO7 does not exhibit methane oxidation activity above that observed for control reactions which do not feature Cu_B (e.g. NeMCO and Con7_3A in Fig. S11). Error bars indicate n = 3 replicates of reaction assay samples.

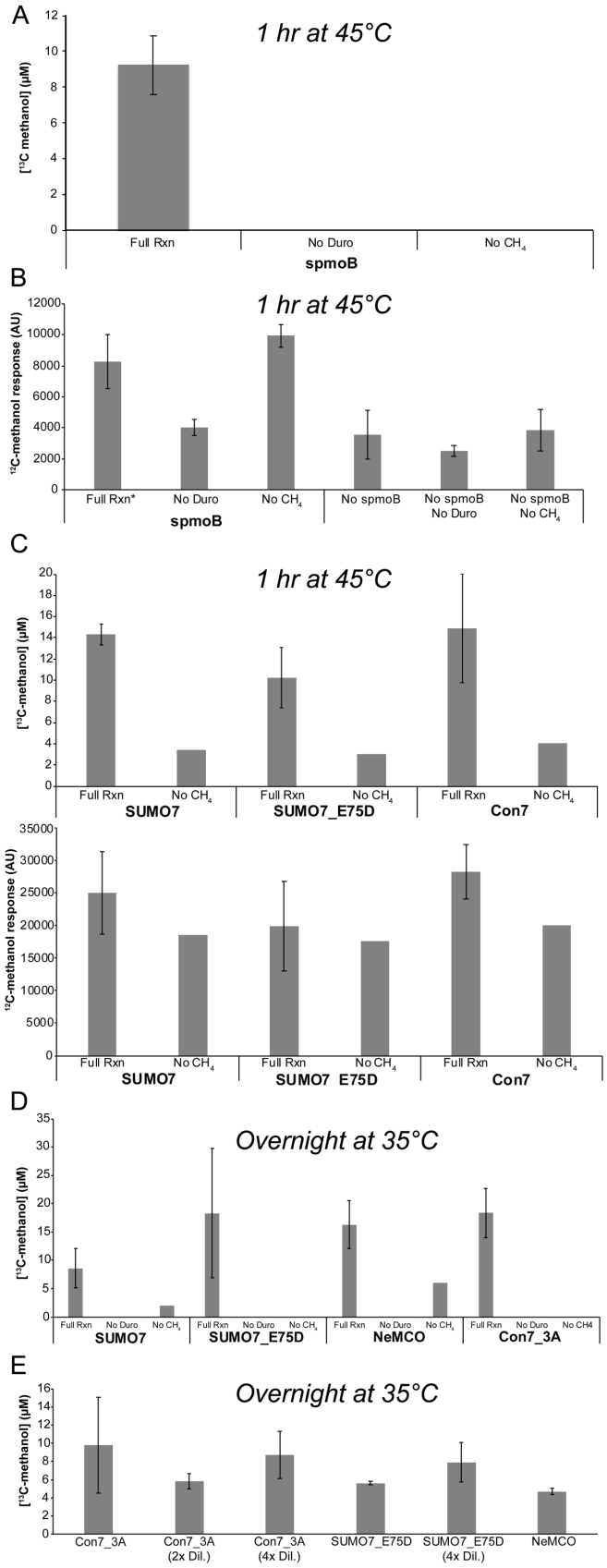
A
1 hr at 45°C
[13C methanol] (μM)
Full Rxn
No Duro
No CH4
spmoB
B
1 hr at 45°C
12C-methanol response (AU)
Full Rxn*
No Duro
No CH4
No spmoB
No spmoB No Duro
No spmoB No CH4
spmoB
C
1 hr at 45°C
[13C-methanol] (μM)
Full Rxn
No CH4
SUMO7
SUMO7_E75D
Con7
12C-methanol response (AU)
SUMO7
SUMO7 E75D
Con7
D
Overnight at 35°C
[13C-methanol] (μM)
SUMO7
SUMO7_E75D
NeMCO
Con7_3A
E
Overnight at 35°C
[13C-methanol] (μM)
Con7_3A
Con7_3A (2x Dil.)
Con7_3A (4x Dil.)
SUMO7_E75D
SUMO7_E75D (4x Dil.)
NeMCO

* For 1 of the 4 "(+) spmoB, Full Rxn" replicates in (**B**), the entire MS-detected elution profile off the GC column was anomalous, so the replicate was omitted.

Fig. S11. Results of ^{13}C-methane oxidation activity assays performed on spmoB, its variants, as well as NeMCO. Representative assays in which appreciable ^{13}C-methanol was observed are shown. There were other assays run under the same conditions in which no samples showed any ^{13}C-methanol. Error bars indicate n ≥ 2 replicates of reaction assay samples. (**A**) Standard spmoB reaction time/temperature (*24*) generates ^{13}C-methanol from ^{13}C-methane, although the spmoB protein concentration (~30 μM) was lower than traditionally assayed for activity (~100 μM). (**B**) The ^{12}C-methanol absolute MS responses are consistently higher in samples containing both spmoB and duroquinol than in conditions with either individually or neither. While the ^{12}C-methanol levels are higher on average in the "(+) protein, No CH_4" than in the "(+) protein, Full Rxn" for this assay, this trend was often reversed, as shown in (**C**). In these such situations, where ^{12}C-methanol was produced over the course of the assay and the "(+) protein, Full Rxn" sample accumulated more ^{12}C-methanol than the "(+) protein, No CH_4" control, the spmoB construct would have appeared active using the GC-FID method of total methanol quantitation, as performed previously (*24, 27*). The differences in ^{12}C-methanol levels for samples containing both spmoB and duroquinol can be attributed to minor differences in the amount of duroquinol added since standard protocol calls for addition of a small scoop of this insoluble compound. Moreover, ^{12}C-methanol is a common contaminant in many buffer reagents. As ^{13}C represents ~1% of natural abundance carbon, we monitored ^{12}C-methanol levels to ensure that any ^{13}C-methanol observed after reaction was a product of methane oxidation, and not merely observation of the natural abundance ^{13}C-methanol from ^{12}C-methanol contamination. The spmoB protein concentration was 100 μM. (**C**) ***Top***: ^{13}C-methanol produced via spmoB construct reaction with ^{13}C-methane, with ***bottom***: ^{12}C-methanol responses. Con7, SUMO7, and SUMO7_E75D protein concentrations were 22 μM, 6 μM, and 17 μM, respectively. (**D**) ^{13}C-methane oxidation activity assays run overnight on several spmoB constructs as well as NeMCO. The activity detected for spmoB variant constructs is comparable to that observed for an unrelated enzyme (NeMCO) or a variant in which all three Cu_B His ligands are replaced with Ala (Con7_3A). SUMO7, SUMO7_E75D, NeMCO, and Con7_3A protein concentrations were 114 μM, 118 μM, 60 μM, and 131 μM, respectively. (**E**) ^{13}C-methane oxidation activity of diluted samples. There is no dependence on protein concentration. Initial Con7_3A, SUMO7_E75D, and NeMCO protein concentrations (prior to dilution) are same as in (**D**).

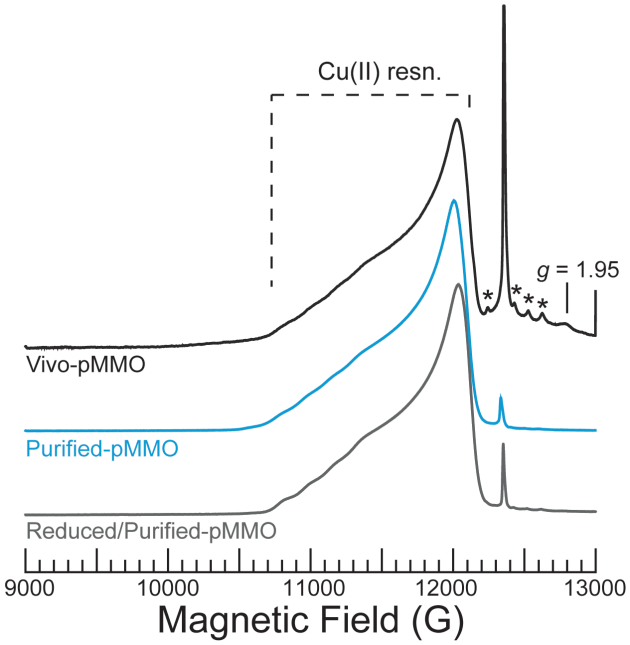

Fig. S12. Rapid-passage Q-band absorption-display CW EPR spectra of the 3 EPR samples shown in Fig. 1 and 2. The Cu(II) resonance is by far the dominant paramagnetic species. We note the extremely weak $g \sim 1.95$ feature in Vivo-pMMO, the intensity of which is exaggerated in the derivative-display of the X-band spectrum in Fig. 1 (~3470 G); this feature contributes negligible integrated intensity. Asterisks denote the hyperfine lines for the small amount of Mn(II) ($I = 5/2$). ***Conditions***: (Purified- and Reduced/Purified-pMMO) ~34.8 GHz microwave frequency, 2 min and 45 second scan rate, 64 ms time constant, 1 G modulation amplitude, temperature ~ 2 K. (Vivo-pMMO) is the same as the others except scan rate was twice as fast.

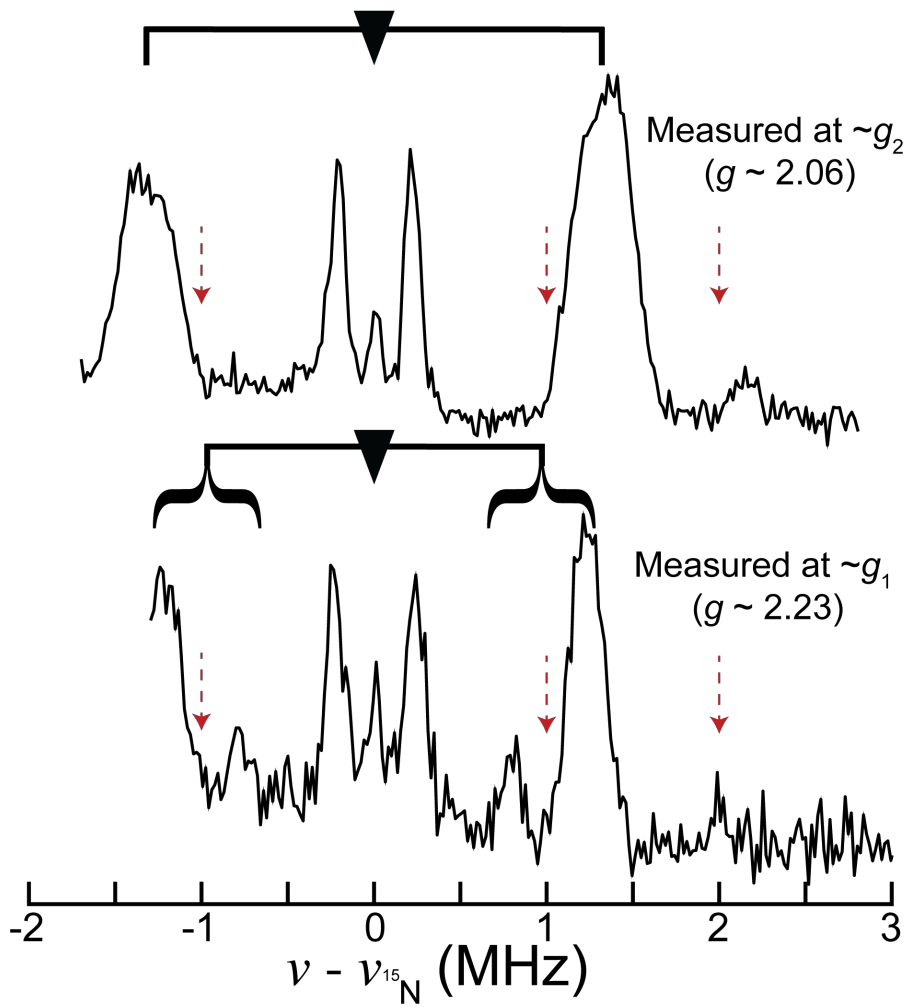

Fig. S13. Vivo-pMMO weakly-coupled ^{15}N Mims ENDOR showing both ν_+ and ν_- resonance, measured at g_1 and g_2. Triangle defines $\nu_{^{15}N}$ and goalpost splittings define ν_+ and ν_- partners; red arrows denote Mims "holes". For the Mims pulse sequence, the ENDOR response (R) is defined by the equation $R \sim 1 - \cos(2\pi A\tau)$. Consequently, for all integer values of $A\tau$ the ENDOR response/intensity is 0, leading to the so-called Mims "holes". For both ^{15}N-Larmor corrected spectra above, τ was chosen such that Mims holes appear every $|A|$ = Z(2 MHz), where Z is an integer. The g_1 ^{15}N ν_+ and ν_- responses both show such Mims holes (at $\nu_{^{15}N}$ ±1 MHz), confirming their assignment to weakly-coupled ^{15}N resonance. We note these must be Mims holes, as Fig. 2 indicates that for appropriate values of τ, ^{15}N resonance is non-zero at this frequency. The microwave amplifier employed for these measurements cannot measure frequencies low enough to observe the full ν_- peak at g_1. Collection conditions: 34.64 GHz microwave frequency, 50 ms repetition time, π = 100 ns, τ = 500 ns, T_{RF} = 60 µs, and RF tail = 10 µs.

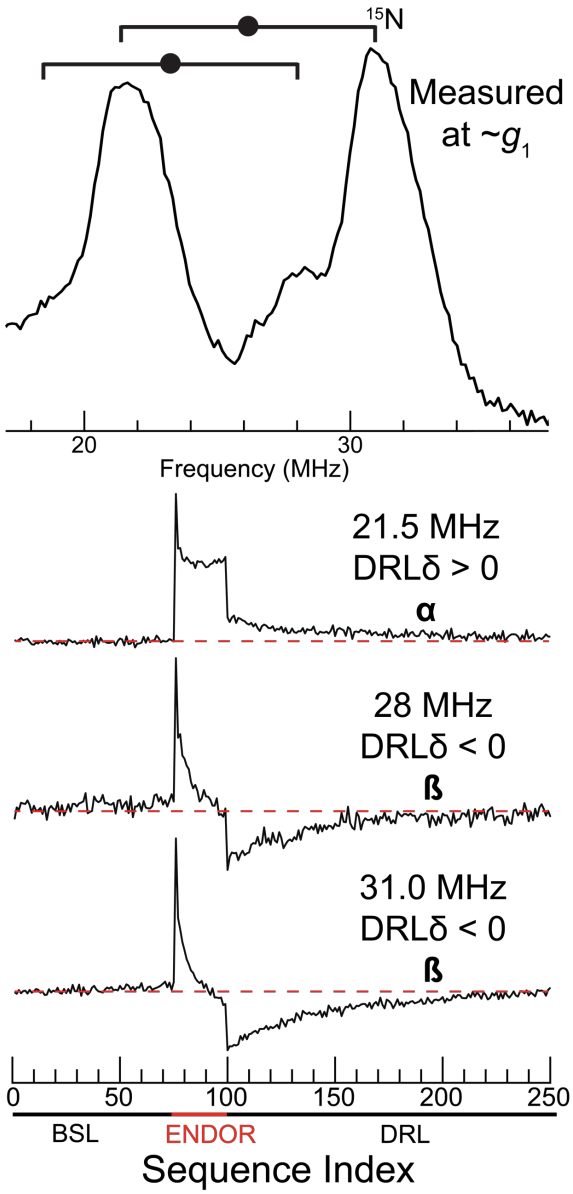

Fig. S14. PESTRE hyperfine sign assignments for strongly-coupled ^{15}N resonance in Vivo-pMMO. ***Top***: Davies ENDOR measurements defining the ^{15}N resonance at g_1. ***Bottom***: PESTRE responses measured at measured at g_1. The PESTRE experiment utilizes three discrete Davies ENDOR sequences. First, a baseline signal is established (BSL) during which time the microwave is applied with no RF, saturating the EPR transition. Next, a single frequency RF is applied to saturate the ENDOR transition (ENDOR). Finally, the RF is turned off (DRL) and the direction of echo relaxation relative to the BSL (DRLδ ≡ DRL - BSL) defines the manifold producing the observed resonance (labeled as α or β to indicate the higher or lower energy electron spin manifolds, respectively). For ν_+ DRLδ > 0, $A/g_n < 0$, while ν_+ DRLδ < 0 defines $A/g_n > 0$; likewise, for ν_- DRLδ < 0, $A/g_n < 0$, while ν_- DRLδ > 0 defines $A/g_n > 0$. Consequently, as expected, the PESTRE measurements are consistent with exclusively strongly-coupled ^{15}N $A/g_n > 0$, indicating a positive spin density $\rho > 0$ since $\rho \propto A/g_n$. Collection conditions: 34.5-34.6 GHz microwave frequency, 100 ms repetition time, π = 80 ns, τ = 600 ns, T_{RF} = 15 µs, and RF tail = 5 µs.

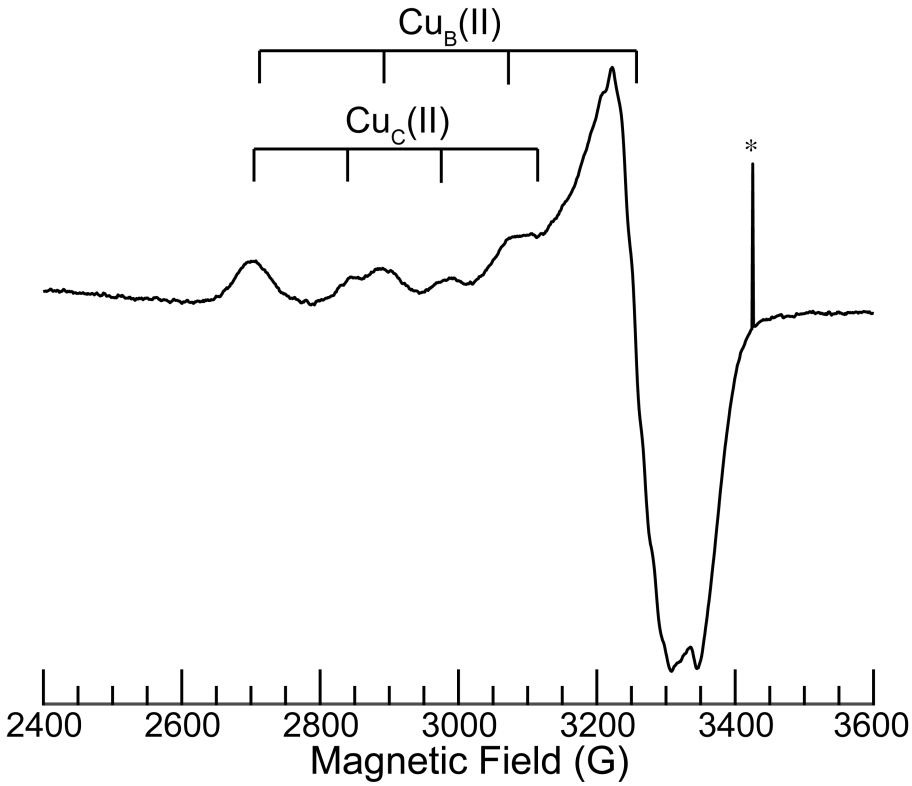

Fig. S15. X-band CW EPR of the Purified-pMMO sample used for DEER measurements (buffer conditions: 50 mM PIPES, 500 mM NaCl, 0.04% DDM, pH 7.2). Bracket width denotes A_1 Cu hyperfine splitting, and the center of the brackets indicate g_1 using the values from Table S1. Asterisk denotes an instrument artifact sometimes observed on the spectrometer. The altered buffer conditions do not alter the Cu_B(II) or Cu_C(II) signals from those observed under the standard Purified-pMMO buffer conditions (as in Fig. 1). Collection conditions: 9.366 GHz microwave frequency, 90 s scan rate, 320 ms time constant, 12.5 G modulation amplitude, 20 K temperature, 5 scans.

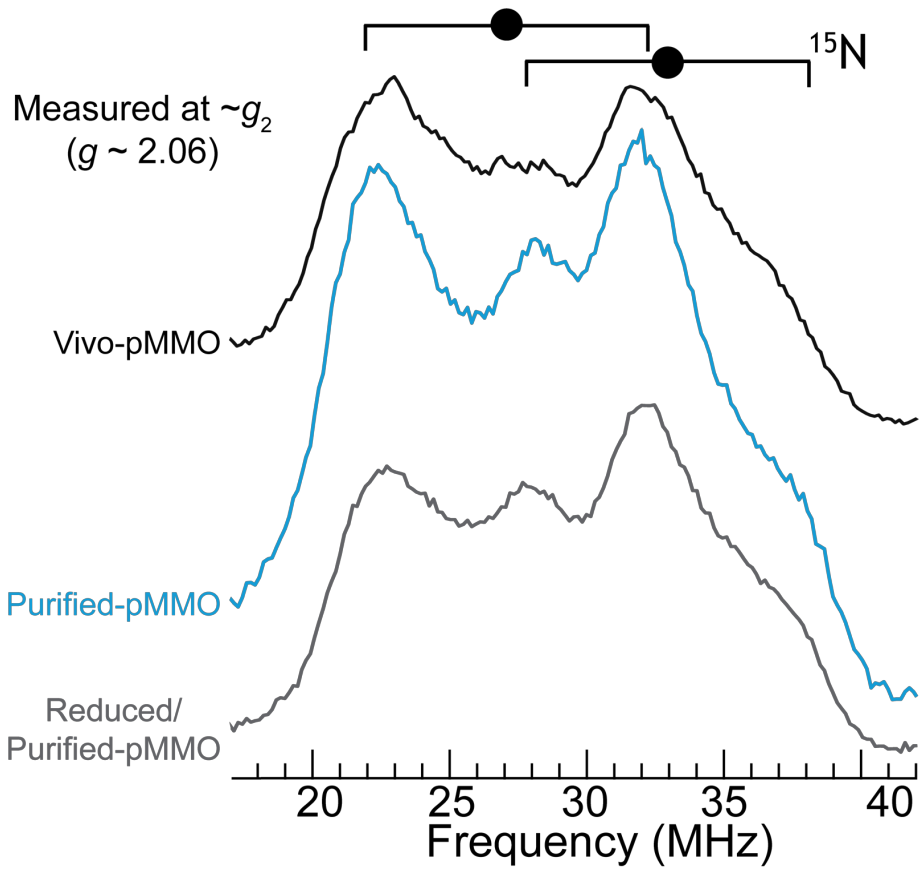

Fig. S16. ^{15}N Davies ENDOR measured at g_2 for Vivo-, Purified-, and Reduced/Purified-pMMO. Intensities normalized to match those of ^{15}N in Fig. S3A. Goalpost width indicates twice the ^{15}N Larmor frequency ($\nu_{^{15}\mathrm{N}}$), filled circle defines half the hyperfine coupling magnitude ($|A/2|$). Collection conditions: 34.5-34.7 GHz microwave frequency, 50 ms repetition time, π = 80 ns, τ = 400 ns, T_{RF} = 15 µs, and RF tail = 5 µs.

References and Notes

1. M. O. Ross, A. C. Rosenzweig, A tale of two methane monooxygenases. *J. Biol. Inorg. Chem.* **22**, 307–319 (2017). doi:10.1007/s00775-016-1419-y Medline

2. A. R. Brandt, G. A. Heath, E. A. Kort, F. O'Sullivan, G. Pétron, S. M. Jordaan, P. Tans, J. Wilcox, A. M. Gopstein, D. Arent, S. Wofsy, N. J. Brown, R. Bradley, G. D. Stucky, D. Eardley, R. Harriss, Energy and environment. Methane leaks from North American natural gas systems. *Science* **343**, 733–735 (2014). doi:10.1126/science.1247045 Medline

3. Environmental Protection Agency (EPA), *Inventory of U.S. greenhouse gas emissions and sinks: 1990–2015* (EPA, 2017).

4. Q. Fei, M. T. Guarnieri, L. Tao, L. M. L. Laurens, N. Dowe, P. T. Pienkos, Bioconversion of natural gas to liquid fuel: Opportunities and challenges. *Biotechnol. Adv.* **32**, 596–614 (2014). doi:10.1016/j.biotechadv.2014.03.011 Medline

5. R. Horn, R. Schlögl, Methane activation by heterogeneous catalysis. *Catal. Lett.* **145**, 23–39 (2015). doi:10.1007/s10562-014-1417-z

6. B. E. R. Snyder, M. L. Bols, R. A. Schoonheydt, B. F. Sels, E. I. Solomon, Iron and copper active sites in zeolites and their correlation to metalloenzymes. *Chem. Rev.* **118**, 2718–2768 (2018). doi:10.1021/acs.chemrev.7b00344 Medline

7. M. S. Khan, J. H. Park, Y. D. Chaniago, M. Lee, Energy efficient process structure design of LNG/NGL recovery for offshore FLNG plant. *Energy Procedia* **61**, 599–602 (2014). doi:10.1016/j.egypro.2014.11.1179

8. J. Gao, Y. Zheng, J.-M. Jehng, Y. Tang, I. E. Wachs, S. G. Podkolzin, Catalysis. Identification of molybdenum oxide nanostructures on zeolites for natural gas conversion. *Science* **348**, 686–690 (2015). doi:10.1126/science.aaa7048 Medline

9. T. J. Lawton, A. C. Rosenzweig, Methane-oxidizing enzymes: An upstream problem in biological gas-to-liquids conversion. *J. Am. Chem. Soc.* **138**, 9327–9340 (2016). doi:10.1021/jacs.6b04568 Medline

10. R. L. Lieberman, A. C. Rosenzweig, Crystal structure of a membrane-bound metalloenzyme that catalyses the biological oxidation of methane. *Nature* **434**, 177–182 (2005). doi:10.1038/nature03311 Medline

11. S. M. Smith, S. Rawat, J. Telser, B. M. Hoffman, T. L. Stemmler, A. C. Rosenzweig, Crystal structure and characterization of particulate methane monooxygenase from *Methylocystis* species strain M. *Biochemistry* **50**, 10231–10240 (2011). doi:10.1021/bi200801z Medline

12. S. Sirajuddin, D. Barupala, S. Helling, K. Marcus, T. L. Stemmler, A. C. Rosenzweig, Effects of zinc on particulate methane monooxygenase activity and structure. *J. Biol. Chem.* **289**, 21782–21794 (2014). doi:10.1074/jbc.M114.581363 Medline

13. S. Y. Ro, M. O. Ross, Y. W. Deng, S. Batelu, T. J. Lawton, J. D. Hurley, T. L. Stemmler, B. M. Hoffman, A. C. Rosenzweig, From micelles to bicelles: Effect of the membrane on particulate methane monooxygenase activity. *J. Biol. Chem.* **293**, 10457–10465 (2018). doi:10.1074/jbc.RA118.003348 Medline

14. R. Balasubramanian, A. C. Rosenzweig, Structural and mechanistic insights into methane oxidation by particulate methane monooxygenase. *Acc. Chem. Res.* **40**, 573–580 (2007). doi:10.1021/ar700004s Medline

15. A. S. Hakemian, K. C. Kondapalli, J. Telser, B. M. Hoffman, T. L. Stemmler, A. C. Rosenzweig, The metal centers of particulate methane monooxygenase from Methylosinus trichosporium OB3b. *Biochemistry* **47**, 6793–6801 (2008). doi:10.1021/bi800598h Medline

16. L. Cao, O. Caldararu, A. C. Rosenzweig, U. Ryde, Quantum refinement does not support dinuclear copper sites in crystal structures of particulate methane monooxygenase. *Angew. Chem. Int. Ed.* **57**, 162–166 (2018). doi:10.1002/anie.201708977 Medline

17. V. C. C. Wang, S. Maji, P. P.-Y. Chen, H. K. Lee, S. S.-F. Yu, S. I. Chan, Alkane oxidation: Methane monooxygenases, related enzymes, and their biomimetics. *Chem. Rev.* **117**, 8574–8621 (2017). doi:10.1021/acs.chemrev.6b00624 Medline

18. H. H. Nguyen, A. K. Shiemke, S. J. Jacobs, B. J. Hales, M. E. Lidstrom, S. I. Chan, The nature of the copper ions in the membranes containing the particulate methane monooxygenase from *Methylococcus capsulatus* (Bath). *J. Biol. Chem.* **269**, 14995–15005 (1994). Medline

19. S. I. Chan, V. C.-C. Wang, J. C.-H. Lai, S. S.-F. Yu, P. P.-Y. Chen, K. H.-C. Chen, C.-L. Chen, M. K. Chan, Redox potentiometry studies of particulate methane monooxygenase: Support for a trinuclear copper cluster active site. *Angew. Chem. Int. Ed.* **46**, 1992–1994 (2007). doi:10.1002/anie.200604647 Medline

20. H. Yuan, M. L. P. Collins, W. E. Antholine, Low-frequency EPR of the copper in particulate methane monooxygenase from *Methylomicrobium albus* BG8. *J. Am. Chem. Soc.* **119**, 5073–5074 (1997). doi:10.1021/ja9701669

21. D. W. Choi, W. E. Antholine, Y. S. Do, J. D. Semrau, C. J. Kisting, R. C. Kunz, D. Campbell, V. Rao, S. C. Hartsel, A. A. DiSpirito, Effect of methanobactin on the activity and electron paramagnetic resonance spectra of the membrane-associated methane monooxygenase in *Methylococcus capsulatus* Bath. *Microbiology* **151**, 3417–3426 (2005). doi:10.1099/mic.0.28169-0 Medline

22. P. Basu, B. Katterle, K. K. Andersson, H. Dalton, The membrane-associated form of methane mono-oxygenase from *Methylococcus capsulatus* (Bath) is a copper/iron protein. *Biochem. J.* **369**, 417–427 (2003). doi:10.1042/bj20020823 Medline

23. R. L. Lieberman, D. B. Shrestha, P. E. Doan, B. M. Hoffman, T. L. Stemmler, A. C. Rosenzweig, Purified particulate methane monooxygenase from *Methylococcus capsulatus* (Bath) is a dimer with both mononuclear copper and a copper-containing cluster. *Proc. Natl. Acad. Sci. U.S.A.* **100**, 3820–3825 (2003). doi:10.1073/pnas.0536703100 Medline

24. M. A. Culpepper, G. E. Cutsail III, W. A. Gunderson, B. M. Hoffman, A. C. Rosenzweig, Identification of the valence and coordination environment of the particulate methane monooxygenase copper centers by advanced EPR characterization. *J. Am. Chem. Soc.* **136**, 11767–11775 (2014). doi:10.1021/ja5053126 Medline

25. J. A. Zahn, A. A. DiSpirito, Membrane-associated methane monooxygenase from Methylococcus capsulatus (Bath). *J. Bacteriol.* **178**, 1018–1029 (1996). doi:10.1128/jb.178.4.1018-1029.1996 Medline

26. M. Martinho, D. W. Choi, A. A. Dispirito, W. E. Antholine, J. D. Semrau, E. Münck, Mössbauer studies of the membrane-associated methane monooxygenase from *Methylococcus capsulatus* bath: Evidence for a Diiron center. *J. Am. Chem. Soc.* **129**, 15783–15785 (2007). doi:10.1021/ja077682b Medline

27. R. Balasubramanian, S. M. Smith, S. Rawat, L. A. Yatsunyk, T. L. Stemmler, A. C. Rosenzweig, Oxidation of methane by a biological dicopper centre. *Nature* **465**, 115–119 (2010). doi:10.1038/nature08992 Medline

28. S. S. Lemos, M. L. Perille Collins, S. S. Eaton, G. R. Eaton, W. E. Antholine, Comparison of EPR-visible Cu^{2+} sites in pMMO from *Methylococcus capsulatus* (Bath) and *Methylomicrobium album* BG8. *Biophys. J.* **79**, 1085–1094 (2000). doi:10.1016/S0006-3495(00)76362-4 Medline

29. U. Sakaguchi, A. W. Addison, *J. Chem. Soc.* 600–608 (1979).

30. R. Pogni, M. C. Baratto, A. Diaz, R. Basosi, EPR characterization of mono(thiosemicarbazones) copper(II) complexes. Note II. *J. Inorg. Biochem.* **79**, 333–337 (2000). doi:10.1016/S0162-0134(99)00166-X Medline

31. R. N. Patel, K. K. Shukla, A. Singh, M. Choudhary, U. K. Chauhan, S. Dwivedi, Copper(II) complexes as superoxide dismutase mimics: Synthesis, characterization, crystal structure and bioactivity of copper(II) complexes. *Inorg. Chim. Acta* **362**, 4891–4898 (2009). doi:10.1016/j.ica.2009.07.037

32. M. Iwaizumi, T. Kudo, S. Kita, Correlation between the hyperfine coupling constants of donor nitrogens and the structures of the first coordination sphere in copper complexes as studied by nitrogen-14 ENDOR spectroscopy. *Inorg. Chem.* **25**, 1546–1550 (1986). doi:10.1021/ic00230a008

33. M. M. Dicus, A. Conlan, R. Nechushtai, P. A. Jennings, M. L. Paddock, R. D. Britt, S. Stoll, Binding of histidine in the $(Cys)_3(His)_1$-coordinated [2Fe-2S] cluster of human mitoNEET. *J. Am. Chem. Soc.* **132**, 2037–2049 (2010). doi:10.1021/ja909359g Medline

34. P. Manikandan, B. Epel, D. Goldfarb, Structure of copper(II)-histidine based complexes in frozen aqueous solutions as determined from high-field pulsed electron nuclear double resonance. *Inorg. Chem.* **40**, 781–787 (2001). doi:10.1021/ic0011361 Medline

35. H. Yokoi, ESR and optical absorption studies of various bis(*N*-salicylidenealkylaminato)copper(II) complexes with tetrahedrallydistorted coordination geometry. *Bull. Chem. Soc. Jpn.* **47**, 3037–3040 (1974). doi:10.1246/bcsj.47.3037

36. T. P. Cheeseman, D. Hall, T. N. Waters, The colour isomerism and structure of copper co-ordination compounds. Part XI. The crystal structure of bis-(N-t-butylsalicylaldiminato)-copper(II). *J. Chem. Soc. A* **1966**, 685–693 (1966). doi:10.1039/j19660000685

37. M. A. Culpepper, G. E. Cutsail III, B. M. Hoffman, A. C. Rosenzweig, Evidence for oxygen binding at the active site of particulate methane monooxygenase. *J. Am. Chem. Soc.* **134**, 7640–7643 (2012). doi:10.1021/ja302195p Medline

38. H. Yuan, M. L. Collins, W. E. Antholine, Concentration of Cu, EPR-detectable Cu, and formation of cupric-ferrocyanide in membranes with pMMO. *J. Inorg. Biochem.* **72**, 179–185 (1998). doi:10.1016/S0162-0134(98)10078-8 Medline

39. G. Jeschke, V. Chechik, P. Ionita, A. Godt, H. Zimmermann, J. Banham, C. R. Timmel, D. Hilger, H. Jung, DeerAnalysis2006—A comprehensive software package for analyzing pulsed ELDOR data. *Appl. Magn. Reson.* **30**, 473–498 (2006). doi:10.1007/BF03166213

40. G. Nyerges, L. Y. Stein, Ammonia cometabolism and product inhibition vary considerably among species of methanotrophic bacteria. *FEMS Microbiol. Lett.* **297**, 131–136 (2009). doi:10.1111/j.1574-6968.2009.01674.x Medline

41. L. Y. Stein, D. J. Arp, Loss of ammonia monooxygenase activity in nitrosomonas europaea upon exposure to nitrite. *Appl. Environ. Microbiol.* **64**, 4098–4102 (1998). Medline

42. M. Fittipaldi, H. J. Wijma, M. P. Verbeet, G. W. Canters, E. J. J. Groenen, M. Huber, The substrate-bound type 2 copper site of nitrite reductase: The nitrogen hyperfine coupling of nitrite revealed by pulsed EPR. *Biochemistry* **44**, 15193–15202 (2005). doi:10.1021/bi0513913 Medline

43. H. J. Op den Camp, T. Islam, M. B. Stott, H. R. Harhangi, A. Hynes, S. Schouten, M. S. M. Jetten, N.-K. Birkeland, A. Pol, P. F. Dunfield, Environmental, genomic and taxonomic perspectives on methanotrophic *Verrucomicrobia*. *Environ. Microbiol. Rep.* **1**, 293–306 (2009). doi:10.1111/j.1758-2229.2009.00022.x Medline

44. C. C. White, R. K. Chain, R. Malkin, Duroquinol as an electron donor for chloroplast electron transfer reactions. *Biochim. Biophys. Acta* **502**, 127–137 (1978). doi:10.1016/0005-2728(78)90137-8 Medline

45. C. E. Taylor, Methanol and hydrogen from methane, water, and light. *Prepr. Pap.-Am. Chem. Soc. Div. Fuel Chem.* **48**, 876 (2003).

46. E. Cadenas, A. Boveris, C. I. Ragan, A. O. M. Stoppani, Production of superoxide radicals and hydrogen peroxide by NADH-ubiquinone reductase and ubiquinol-cytochrome c reductase from beef-heart mitochondria. *Arch. Biochem. Biophys.* **180**, 248–257 (1977). doi:10.1016/0003-9861(77)90035-2 Medline

47. H. Ikai, K. Nakamura, M. Shirato, T. Kanno, A. Iwasawa, K. Sasaki, Y. Niwano, M. Kohno, Photolysis of hydrogen peroxide, an effective disinfection system via hydroxyl radical formation. *Antimicrob. Agents Chemother.* **54**, 5086–5091 (2010). doi:10.1128/AAC.00751-10 Medline

48. E. F. Liew, D. Tong, N. V. Coleman, A. J. Holmes, Mutagenesis of the hydrocarbon monooxygenase indicates a metal centre in subunit-C, and not subunit-B, is essential for copper-containing membrane monooxygenase activity. *Microbiology* **160**, 1267–1277 (2014). doi:10.1099/mic.0.078584-0 Medline

49. H. Yuan, M. L. P. Collins, W. E. Antholine, Type 2 Cu^{2+} in pMMO from Methylomicrobium album BG8. *Biophys. J.* **76**, 2223–2229 (1999). doi:10.1016/S0006-3495(99)77378-9 Medline

50. C. D. Blanchette, J. M. Knipe, J. K. Stolaroff, J. R. DeOtte, J. S. Oakdale, A. Maiti, J. M. Lenhardt, S. Sirajuddin, A. C. Rosenzweig, S. E. Baker, Printable enzyme-embedded

materials for methane to methanol conversion. *Nat. Commun.* **7**, 11900 (2016). doi:10.1038/ncomms11900 Medline

51. S. Cabantous, G. S. Waldo, In vivo and in vitro protein solubility assays using split GFP. *Nat. Methods* **3**, 845–854 (2006). doi:10.1038/nmeth932 Medline

52. Y.-B. Zhang, J. Howitt, S. McCorkle, P. Lawrence, K. Springer, P. Freimuth, Protein aggregation during overexpression limited by peptide extensions with large net negative charge. *Protein Expr. Purif.* **36**, 207–216 (2004). doi:10.1016/j.pep.2004.04.020 Medline

53. M. P. DeLisa, D. Tullman, G. Georgiou, Folding quality control in the export of proteins by the bacterial twin-arginine translocation pathway. *Proc. Natl. Acad. Sci. U.S.A.* **100**, 6115–6120 (2003). doi:10.1073/pnas.0937838100 Medline

54. A. C. Fisher, W. Kim, M. P. DeLisa, Genetic selection for protein solubility enabled by the folding quality control feature of the twin-arginine translocation pathway. *Protein Sci.* **15**, 449–458 (2006). doi:10.1110/ps.051902606 Medline

55. J. Li, T. J. Lawton, J. S. Kostecki, A. Nisthal, J. Fang, S. L. Mayo, A. C. Rosenzweig, M. C. Jewett, Cell-free protein synthesis enables high yielding synthesis of an active multicopper oxidase. *Biotechnol. J.* **11**, 212–218 (2016). doi:10.1002/biot.201500030 Medline

56. F. W. Studier, Protein production by auto-induction in high density shaking cultures. *Protein Expr. Purif.* **41**, 207–234 (2005). doi:10.1016/j.pep.2005.01.016 Medline

57. S. Stoll, A. Schweiger, EasySpin, a comprehensive software package for spectral simulation and analysis in EPR. *J. Magn. Reson.* **178**, 42–55 (2006). doi:10.1016/j.jmr.2005.08.013 Medline

58. C. E. Davoust, P. E. Doan, B. M. Hoffman, Q-Band Pulsed Electron Spin-Echo Spectrometer and Its Application to ENDOR and ESEEM. *J. Magn. Reson. A* **119**, 38–44 (1996). doi:10.1006/jmra.1996.0049

59. B. Epel, I. Gromov, S. Stoll, A. Schweiger, D. Goldfarb, Spectrometer manager: A versatile control software for pulse EPR spectrometers. *Concepts Magn. Reson. Part B Magn. Reson. Eng.* **26B**, 36–45 (2005). doi:10.1002/cmr.b.20037

60. P. E. Doan, B. M. Hoffman, Making hyperfine selection in Mims ENDOR independent of deadtime. *Chem. Phys. Lett.* **269**, 208–214 (1997). doi:10.1016/S0009-2614(97)00293-5

61. P. E. Doan, Combining steady-state and dynamic methods for determining absolute signs of hyperfine interactions: Pulsed ENDOR Saturation and Recovery (PESTRE). *J. Magn. Reson.* **208**, 76–86 (2011). doi:10.1016/j.jmr.2010.10.008 Medline

62. N. C. Eickman, R. S. Himmelwright, E. I. Solomon, Geometric and electronic structure of oxyhemocyanin: Spectral and chemical correlations to met apo, half met, met, and dimer active sites. *Proc. Natl. Acad. Sci. U.S.A.* **76**, 2094–2098 (1979). doi:10.1073/pnas.76.5.2094 Medline

63. M. Pretzler, A. Rompel, What causes the different functionality in type-III-copper enzymes? A state of the art perspective. *Inorg. Chim. Acta* **481**, 25–31 (2018). doi:10.1016/j.ica.2017.04.041

64. R. J. Gurbiel, Y. C. Fann, K. K. Surerus, M. M. Werst, S. M. Musser, P. E. Doan, S. I. Chan, J. A. Fee, B. M. Hoffman, Detection of two histidyl ligands to CuA of cytochrome oxidase by 35-GHz ENDOR. ^{14,15}N and ^{63,65}Cu ENDOR studies of the CuA site in bovine heart cytochrome aa3 and cytochromes caa3 and ba3 from Thermus thermophilus. *J. Am. Chem. Soc.* **115**, 10888–10894 (1993). doi:10.1021/ja00076a053

65. N. Atherton, A. Horsewill, Proton ENDOR of $Cu(H_2O)_6^{2+}$ in $Mg(NH_4)_2(SO_2)_4$. $6H_2O$. *Mol. Phys.* **37**, 1349–1361 (1979). doi:10.1080/00268977900100991

66. H. Goldenberg, L. Jirovetz, P. Krajnik, W. Mosgoeller, T. Moslinger, E. Schweinzer, Quantitation of dehydroascorbic acid by the kinetic measurement of a derivatization reaction. *Anal. Chem.* **66**, 1086–1089 (1994). doi:10.1021/ac00079a025

67. D. Getz, B. L. Silver, ESR of $Cu^{2+}(H_2O)_6$. I. The oxygen-17 superhyperfine tensors in ^{63}Cu $^{2+}$ doped zinc Tutton's salt at 20 °K. *J. Chem. Phys.* **61**, 630–637 (1974). doi:10.1063/1.1681939

68. D. Kim, N. H. Kim, S. H. Kim, 34 GHz pulsed ENDOR characterization of the copper coordination of an amyloid β peptide relevant to Alzheimer's disease. *Angew. Chem. Int. Ed.* **52**, 1139–1142 (2013). doi:10.1002/anie.201208108 Medline